



Daily and Subdaily Wind and Divergence Variations Observed by a Shipborne Doppler Radar off the Southwestern Coast of Sumatra

BIAO GENG^a AND MASAKI KATSUMATA^a

^a Center for Coupled Ocean-Atmosphere Research, JAMSTEC, Yokosuka, Japan

(Manuscript received 9 August 2022, in final form 6 February 2023, accepted 15 February 2023)

ABSTRACT: This study investigated the daily cycle of the wind and divergence fields observed off the southwestern coast of Sumatra during a field campaign of the Years of the Maritime Continent pilot study. An algorithm was developed to retrieve kinematic variables from the single-Doppler data collected aboard the Research Vessel *Mirai* from 24 November to 13 December 2015. The observed daily cycles of the wind and divergence fields consisted of diurnal, semidiurnal, and short-term variations. Diurnal wind variation was characterized by deep and three-dimensional circulation. There was an approximate phase locking of the semidiurnal variation to the diurnal variation, both in the wind and divergence fields. The short-term wind variation occurred at a time scale of $\sim 1\text{--}3$ h, and this pattern was associated with density currents or mesoscale gravity waves. Up to 73% of the daily vertical motion variance can be attributed to the diurnal and semidiurnal vertical motion variations with comparable strengths. Concurrently, precipitation propagated offshore in phase with density currents and mesoscale gravity waves. Our results suggest that diurnal and semidiurnal wind variations dominate the daily evolution of precipitation, whereas density currents and mesoscale gravity waves control offshore propagation. Additionally, it appears that the daily precipitation cycle is modulated by multiple-time-scale wind variabilities of less than a day, which is also responsible for the development of strong nocturnal convection off the southwestern coast of Sumatra.

SIGNIFICANCE STATEMENT: To improve our understanding of the daily wind and divergence cycle off the southwestern coast of Sumatra, we examined wind data collected by a shipborne Doppler radar. The observed daily cycles of the wind and divergence fields consisted of diurnal and semidiurnal variations, as well as a 1–3-h variation associated with a density current or mesoscale gravity wave. Our results suggest that diurnal and semidiurnal wind variations dominate the daily evolution of precipitation, whereas density currents and mesoscale gravity waves control offshore propagation. Thus, we highlight the role of multiple-time-scale wind variabilities of less than a day in modulating the daily precipitation cycle off the southwestern coast of Sumatra.


KEYWORDS: Atmosphere; Maritime Continent; Precipitation; Wind; Diurnal effects

1. Introduction

Low-level convergence is one of the key dynamic forces driving deep convection in the tropics (Cotton and Anthes 1989). Convergence induced by daily wind oscillations favors the evolution of convection and precipitation on a diurnal scale, which is a fundamental mode of the global climate system. In particular, diurnal convective activity over the Maritime Continent generates a large amount of heat, which is regarded as a significant source of energy that drives large-scale atmospheric circulation (Ramage 1968).

Atmospheric migrating and nonmigrating tides can generate diurnal and semidiurnal wind oscillations (Chapman and Lindzen 1970; Haurwitz and Cowley 1973). Migrating tides propagate globally, and their phases are independent of longitude and can be expressed in local time. In contrast, nonmigrating tides are locally driven and their phases depend on both local time and longitude. The classical theory of atmospheric tides comprehensively delves into diurnal and semidiurnal pressure and wind variations induced by migrating tides (Carlson and Hastenrath 1970; Chapman and Lindzen 1970; Haurwitz and Cowley 1973).

Observational studies have illustrated the characteristics of diurnal and semidiurnal variations in wind and divergence fields worldwide. By analyzing wind data from the moored buoy array over the tropical Pacific Ocean, Deser (1994), Deser and Smith (1998), and Ueyama and Deser (2008) found that the semidiurnal cycle associated with the migrating tides dominates for the zonal wind, while the locally forced diurnal

 Denotes content that is immediately available upon publication as open access.

Corresponding author: Biao Geng, bgeng@jamstec.go.jp

DOI: 10.1175/JAS-D-22-0170.1

© 2023 American Meteorological Society. For information regarding reuse of this content and general copyright information, consult the AMS Copyright Policy (www.ametsoc.org/PUBSReuseLicenses).

cycle dominates for the meridional wind. Winds observed by wind profilers in the equatorial western and southern Pacific regions also exhibit consistency between the semidiurnal zonal wind and the migrating tidal wind field (Gutzler and Hartten 1995; Hartten and Datulayta 2004). Williams and Avery (1996) found that the wind profiler–observed diurnal wind variation off the equator of the tropical Pacific was induced by tidal mode forcing, whereas the diurnal winds near the equator were more locally forced.

The products of scatterometer observations have been used to reveal diurnal surface wind variations over global oceans (Gille et al. 2005; Brown et al. 2017; Kilpatrick et al. 2017; Short et al. 2019). The sea and land breezes propagated offshore and reached several hundred kilometers off the coast. The offshore propagation speeds ranged from ~ 2 to 30 m s^{-1} , which is consistent with those of density currents or gravity waves (Simpson 1969; Rotunno 1983; Mapes et al. 2003; Tulich and Mapes 2008). Density currents and diurnal gravity waves have been observed to account for the offshore propagation of precipitation over coastal regions (Mori et al. 2004; Li and Carbone 2015; Yokoi et al. 2017; Short et al. 2019; Bai et al. 2021). However, because of their coarse temporal resolution (2–4 times a day), scatterometer observations cannot capture semidiurnal wind variations.

Dai and Deser (1999) documented diurnal and semidiurnal variations in surface wind and divergence fields across the globe based on wind observations from land and island stations along with marine reports from the Comprehensive Ocean–Atmosphere Dataset. Their results indicated a stronger diurnal wind cycle over land than over ocean. Wood et al. (2009) further observed that the diurnal oscillation of the surface divergence field over oceans is largest near tropical landmasses and decreases exponentially away from the coast. Dai and Deser (1999) reported a land–ocean phase difference in the diurnal variation of the surface divergence field. They noted that surface convergence and divergence prevailed over the continents and adjacent oceans, respectively, in the afternoon and early evening. However, the opposite pattern occurred in the early morning. A similar dipole of surface divergence between land and ocean was also observed in the tropical Atlantic Ocean by Christophersen et al. (2020).

Dai and Deser (1999) suggested that this type of land–ocean phase difference in diurnal divergence variation implies the existence of a large-scale diurnal circulation; its ascent branch and descent branch is situated over the continents and nearby oceans in the afternoon and early evening, respectively. Similarly, the opposite is true in the early morning. They concluded that the land–ocean phase difference of the diurnal divergence variation is attributed to distinct pressure gradients, which are induced by daytime higher surface temperature and nighttime colder surface temperature over land than over the ocean. This conclusion is consistent with the results of Dai and Wang (1999), who investigated diurnal and semidiurnal surface-pressure variations. In addition, Dai and Wang (1999) highlighted that the land–sea difference in semidiurnal pressure variation is small. Dai (2001) indicated that the abovementioned diurnal land–ocean circulation favors diurnal variation in precipitation over oceans adjacent to

continents. On the other hand, the low-level divergence field and associated vertical motions resulting from semidiurnal pressure tides are responsible for the semidiurnal variation in precipitation over the tropical oceans (Brier and Simpson 1969; Dai 2001).

Although they have been illustrated in various regions worldwide, diurnal and semidiurnal wind variations and their induced divergence fields have not been documented off the western and southwestern coasts of Sumatra. In these regions, the annual mean rainfall is as high as 4000 mm, with most of the rainfall occurring at night (Mori et al. 2004; Wu et al. 2009; Tan et al. 2019; Worku et al. 2019; Minobe et al. 2020; Sakaeda et al. 2020). Previous studies have proposed that either the land breeze, terrain-induced katabatic flow, or diurnal gravity waves may be responsible for the development of the diurnal cycle of offshore precipitation over the Maritime Continent (Mori et al. 2004; Wu et al. 2009; Love et al. 2011; Hassim et al. 2016; Vincent and Lane 2016; Yokoi et al. 2017; Wei et al. 2020; Bai et al. 2021). However, the process dominating the diurnal variation of offshore precipitation is still disputable. Because low-level convergence and associated updrafts are the most fundamental forces driving deep convection in the tropics, observations of the daily cycle of the wind, divergence, and vertical motion fields off the western and southwestern coasts of Sumatra should broaden our understanding of the daily evolution of convection and precipitation in these regions. In fact, by evaluating numerical model results with observational data, Dipankar et al. (2019) and Lee et al. (2021) indicated that a bias in local circulation produces an unrealistic simulation, whereas an improved representation of local winds sufficiently improves the simulation of diurnal precipitation in the coastal region of Sumatra.

A pronounced diurnal variation in precipitation off the southwestern coast of Sumatra has been observed by the Research Vessel *Mirai* during the field campaign of the Years of the Maritime Continent (YMC) pilot study (Pre-YMC) (Yokoi et al. 2017; Yoneyama and Zhang 2020; Geng et al. 2020). Therefore, the purpose of this study was to investigate the daily cycle of the wind and divergence fields over the sea and its relationship to the development of offshore precipitation observed by the *Mirai* during the Pre-YMC campaign. The remainder of this paper is organized as follows: section 2 describes the data and methods; section 3 presents the results; finally, summary and discussion are presented in section 4.

2. Data and methodology

a. Data

Doppler radar data obtained aboard the *Mirai* during the Pre-YMC campaign were used to investigate the daily cycle of the wind and divergence fields off the southwestern coast of Sumatra. The surface and radiosonde data observed aboard the *Mirai*, the surface data obtained from an automatic weather station installed at the Bengkulu meteorological station of Indonesia, and the hourly European Centre for Medium-Range Weather Forecasts fifth-generation reanalysis (ERA5) data (Hersbach et al. 2020) were used to

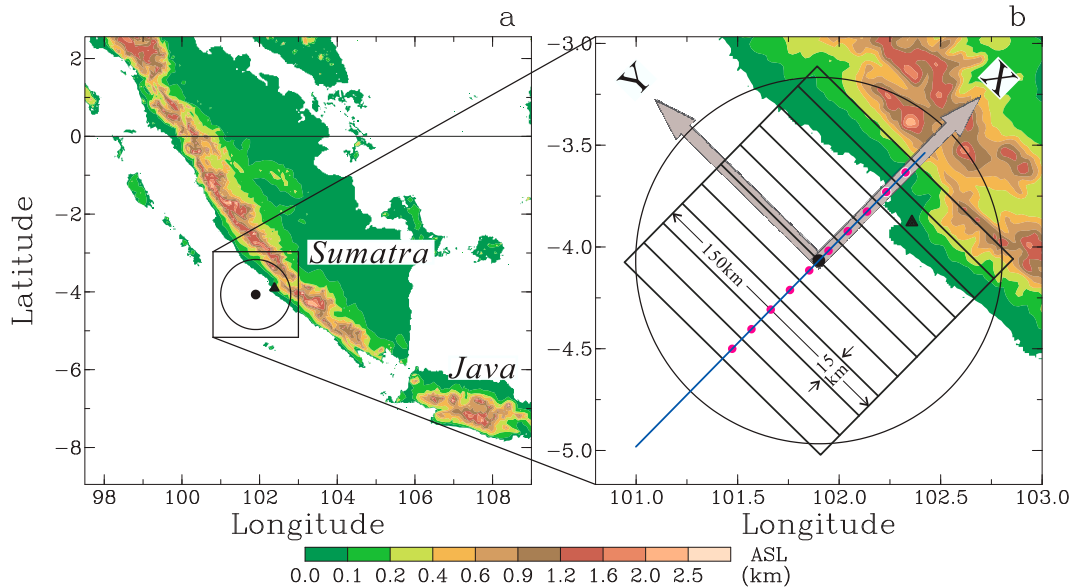


FIG. 1. (a) Topographical map of the study area. The filled black circle and triangle indicate the locations of the Research Vessel *Mirai* and the Bengkulu meteorological station, respectively. The open circle with a radius of 100 km from the Research Vessel *Mirai* shows the range of the radar data. (b) The coordinate system used for retrieving winds from the *Mirai* radar data. The radar data within each box were used to retrieve the wind field at the center (i.e., the filled magenta circle) of the box through a regression analysis. The centers of the boxes were along the x axis, that is, perpendicular to the coast. The cyan line through the centers of the boxes indicates the location where time–distance diagrams derived from the ERA5 data (Figs. 10c,d and 14) are prepared.

validate the Doppler radar results. Figure 1 shows the locations of the *Mirai* and the Bengkulu station. The main specifications of the *Mirai* radar and quality control of the radar data were described by Geng and Katsumata (2020). Radiosonde observations were conducted every 3 h, and the *Mirai* radar performed volume scans every 6 min. Data observed during the period from 0000 UTC 24 November to 0000 UTC 13 December 2015, when diurnal variations in the wind field and precipitation were pronounced over the observation site (Yokoi et al. 2017; Geng et al. 2020), were analyzed in this study. Data after 13 December were not used in this study as the diurnal variation of precipitation turned indistinct (Yokoi et al. 2017), due to the passage over the study area of intensive convective activity associated with a Madden–Julian oscillation (MJO) (Madden and Julian 1972) event.

b. Retrieval of kinematic variables from the Mirai radar

A coordinate system with the x axis and y axis perpendicular and parallel to the coast was utilized (Fig. 1b). The origin of the coordinate system was the *Mirai* radar. The radar data within each box shown in Fig. 1b were used to retrieve the wind field at the center of the box through a regression analysis. As indicated by the filled magenta circles in Fig. 1b, the centers of these boxes were along the x axis, that is, perpendicular to the coast. The x , y , and z dimensions of the box were set to 150 km, 15 km, and 500 m, respectively. The long box parallel to the coast allowed the study of the daily cycle of the along-coast mean kinematic structure perpendicular to the coast.

Similar to previous studies (Easterbrook 1975; Waldteufel and Corbin 1979; Koscielny et al. 1982; Johnston et al. 1990), the wind retrieval was based on the assumption of the linearity of the vector wind field. The relationship between the radial velocity V_r measured by a Doppler radar located at the coordinate origin and the three-dimensional Cartesian velocities (u , v , w) at a point (x , y , z) can be expressed as (Armijo 1969)

$$rV_r = ux + vy + wz, \tag{1.1}$$

where

$$r = (x^2 + y^2 + z^2)^{1/2}. \tag{1.2}$$

Here, w represents the combination of air and hydrometeor vertical motions. The wind field at each point shown by the filled magenta circle in Fig. 1b, which is specified as (x_0, y_0, z_0) , was retrieved by assuming that the three-dimensional velocities varied linearly around that point. Furthermore, u , v , and w in Eq. (1) can be expanded in a Taylor series with respect to (x_0, y_0, z_0) as follows:

$$u = u_0 + u_x(x - x_0) + u_y(y - y_0) + u_z(z - z_0), \tag{2.1}$$

$$v = v_0 + v_x(x - x_0) + v_y(y - y_0) + v_z(z - z_0), \tag{2.2}$$

$$w = w_0 + w_x(x - x_0) + w_y(y - y_0) + w_z(z - z_0), \tag{2.3}$$

where u_0 , y_0 , and w_0 are the three-dimensional velocities at points (x_0, y_0, z_0) .

It is a common practice to exclude small kinematic variables that are not of interest because the estimation of all the parameters shown in Eq. (2) requires a much larger analysis volume (Koscielny et al. 1982). Based on the analyses of previous studies (Waldteufel and Corbin 1979; Johnston et al. 1990) and our own tests, we eliminated the terms w_x , w_y , and w_z , which exerted less influence on the wind-retrieval results. Contamination of u_0 and v_0 by horizontal vorticity occurs when (x_0, y_0) is not centered at the radar site (Easterbrook 1975; Koscielny et al. 1982). In this study, wind retrievals were performed with respect to the points (i.e., the filled magenta circles in Fig. 1b) located on the x axis, $y_0 = 0$. In addition, as diurnal precipitation off the southwestern coast of Sumatra usually develops parallel to the coast, that is, the y axis in Fig. 1b (Geng et al. 2020), the term u_y was further eliminated according to the two-dimensionality of the precipitation feature.

Based on the above conditions and assumptions, Eqs. (1) and (2) were combined and arranged as follows:

$$rV_r = u_0x + v_0y + w_0z + u_x(x^2 - x_0x) + v_yy^2 + v_x(xy - x_0y) + u_zx(z - z_0) + v_zy(z - z_0). \quad (3)$$

Equation (3) was used to retrieve the wind field through a method involving singular value decomposition (Golub and Van Loan 1996). To ensure the accuracy of the results, wind retrieval was performed below a height of 6 km, which is the modal echo-top height of most precipitation systems observed during the Pre-YMC campaign (Geng and Katsumata 2021). For a typical volume scan at heights where the masking effects of Earth's curvature are less pronounced, the number of radar gates contained in the analysis box shown in Fig. 1b varied from ~6000 to over 180 000. The wind retrieval in a box was performed if the number of available data in that box was larger than 500, which appeared to be a sufficient number to perform the regression analysis. The iterative method of Matejka and Srivastava (1991) was used until the residual standard error of V_r in each box was $<1.5 \text{ m s}^{-1}$, which has sufficiently removed the Doppler velocity outliers from the regression analysis.

c. Retrieval of the daily cycle

A temporal anomaly was used to investigate the daily cycle of kinematic variables (Brown et al. 2017; Liang and Wang 2017). Temporal anomaly was calculated by subtracting the mean of each variable during the analysis period. The daily cycle was later constructed by averaging the temporal anomalies at individual local times with an interval of 30 min for the surface and radar data, 1 h for the ERA5 data, and 3 h for the radiosonde data. Finally, the vertical motion of air was determined by vertically integrating the horizontal divergence from the surface upward without establishing upper-boundary conditions. This method may result in vertical motion errors that increase with height, resulting in unreliable vertical motion in the upper regions. To ensure the accuracy of the results, the computation of the vertical motion was terminated at a height of 4.5 km, based on the suggestion of Wang (2004).

3. Results

a. Bulk characteristics of the daily cycle over the radar domain

Time–height diagrams of the daily cycle of the kinematic variables are shown in Fig. 2. The radar-derived zonal wind (Fig. 2a) exhibited a marked diurnal variation, which was dominated by westerly winds at ~1000–1700 local time (LT; LT = UTC + 7 h) and easterly winds at ~1800–0200 LT. In contrast, westerly and easterly winds were also observed at ~0300–0700 and ~0700–1000 LT, respectively, indicating that the zonal wind underwent a semidiurnal oscillation. The radar-derived meridional wind (Fig. 2b) also exhibited pronounced diurnal and semidiurnal variations. The radar-derived diurnal and semidiurnal wind variations were generally consistent with those observed by the radiosondes (Figs. 2c,d). However, because of their coarse temporal resolution, radiosonde observations exhibited smoother diurnal and semidiurnal signals compared to radar observations.

Figures 2e and 2f indicate that radar-derived divergence and downdrafts dominated in the morning and afternoon hours (~0800–1700 LT), whereas convergence and updrafts prevailed during the evening and early night hours (~1800–0000 LT). In addition, relatively strong convergence and updrafts were observed during the early morning around 0600–0800 LT. These facts indicate the existence of diurnal and semidiurnal variations in the divergence and vertical motion fields. The diurnal and semidiurnal variations of each kinematic variable, as shown in Fig. 2, demonstrated a near-constant phase in the low and middle troposphere at most times of the day. Perturbations with shorter time scales of ~1–3 h also existed, which were more prominent in the divergence and vertical motion fields.

Figures 3a and 3b show the daily cycle of the radar-derived zonal and meridional winds, respectively, averaged over the radar domain at 0.75-km height, which was the lowest height at which the distortion of the radar measurement due to Earth curvature could be ignored. The daily cycle of surface winds observed aboard the *Mirai* was superimposed on these figures. The radar-derived zonal and meridional winds were in good agreement with those observed at the surface and both displayed similar diurnal and semidiurnal oscillations. Harmonic analyses (Chapman and Lindzen 1970) were used to extract the diurnal and semidiurnal cycle components of the wind field observed using the *Mirai* radar.

The maximum amplitudes of the diurnal zonal and meridional wind harmonics were 0.83 m s^{-1} at 1230 LT and 1.36 m s^{-1} at 1800 LT, respectively (Figs. 3a,b). For the semidiurnal harmonics, the maximum zonal and meridional winds were 0.53 m s^{-1} at 0300/1500 LT and 0.8 m s^{-1} at 0600/1800 LT, respectively. As indicated by the squared correlation coefficient (R^2) in Figs. 3a and 3b, the diurnal and semidiurnal harmonics explained 55% and 23%, respectively, of the zonal wind variance, whereas they accounted for 69% and 25%, respectively, of the meridional wind variance. This result implies the dominance of the diurnal variation over the semidiurnal variation in both the zonal wind and meridional wind, which is different from previous observations across the tropical Pacific that

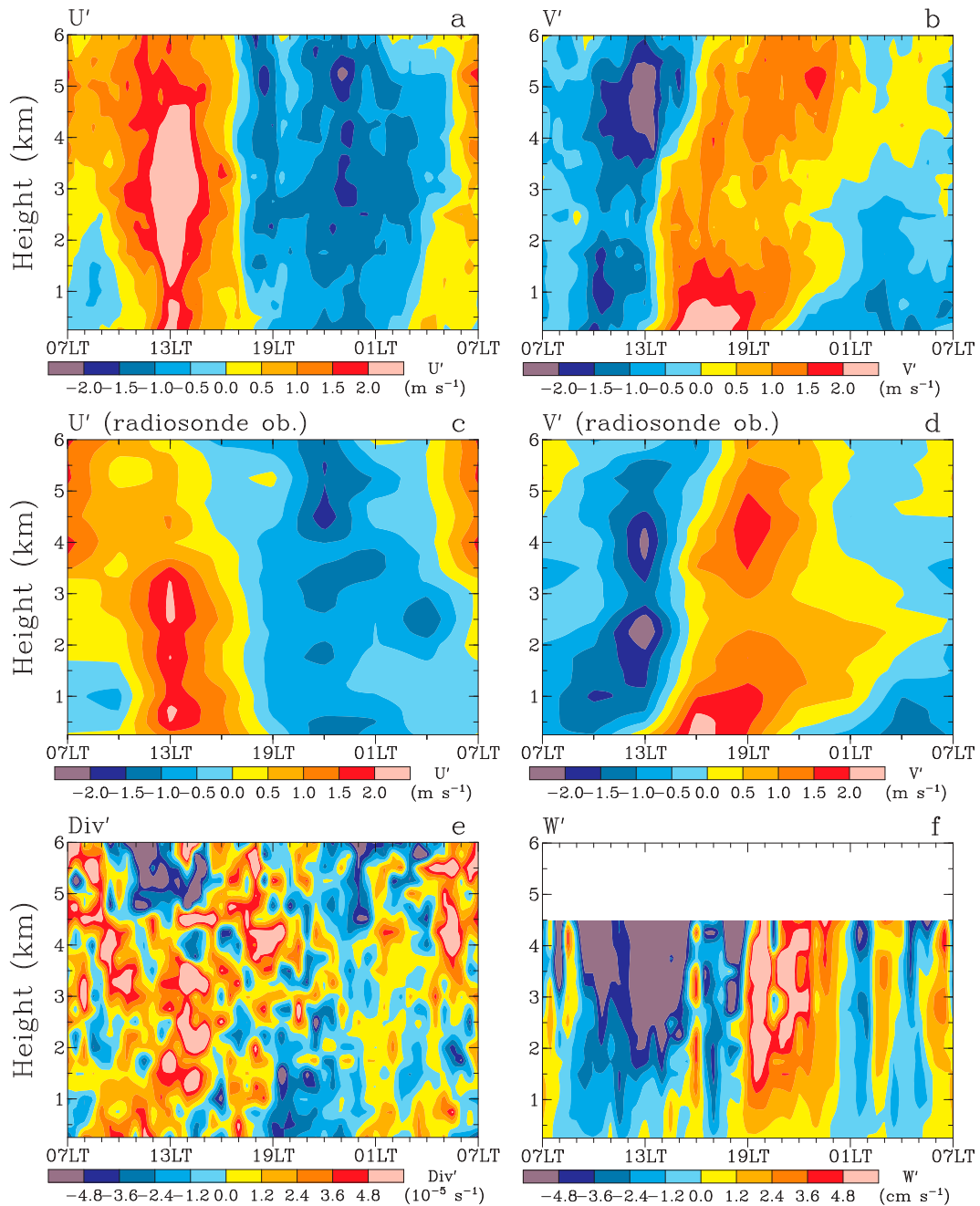


FIG. 2. (a),(b) Time–height diagrams of the daily cycle of (a) zonal wind anomalies and (b) meridional wind anomalies (color shades; m s^{-1}) derived from the radar data and averaged over the radar domain. (c),(d) As in (a) and (b), but for (c) zonal wind anomalies and (d) meridional wind anomalies (color shades; m s^{-1}) derived from the radiosonde data. For the sake of comparison with the radar results, the radiosonde data were not used when the occurrence frequency with reflectivity values of ≥ 10 dBZ derived from the radar data and averaged over the radar domain was less than 3%. (e),(f) As in (a) and (b), but for (e) divergence anomalies (color shades; 10^{-5} s^{-1}) and (f) vertical motion anomalies (color shades; cm s^{-1}) derived from the radar data and averaged over the radar domain.

demonstrated the dominance of the semidiurnal cycle of the zonal wind over its diurnal cycle (Deser 1994; Deser and Smith 1998; Harten and Datulayta 2004; Ueyama and Deser 2008). The diurnal and semidiurnal harmonics jointly explained 78%

of the zonal wind variance and 94% of the meridional wind variance.

The daily cycle of sea level pressure observed aboard the *Mirai* is shown in Fig. 3c. The maximum amplitude of the

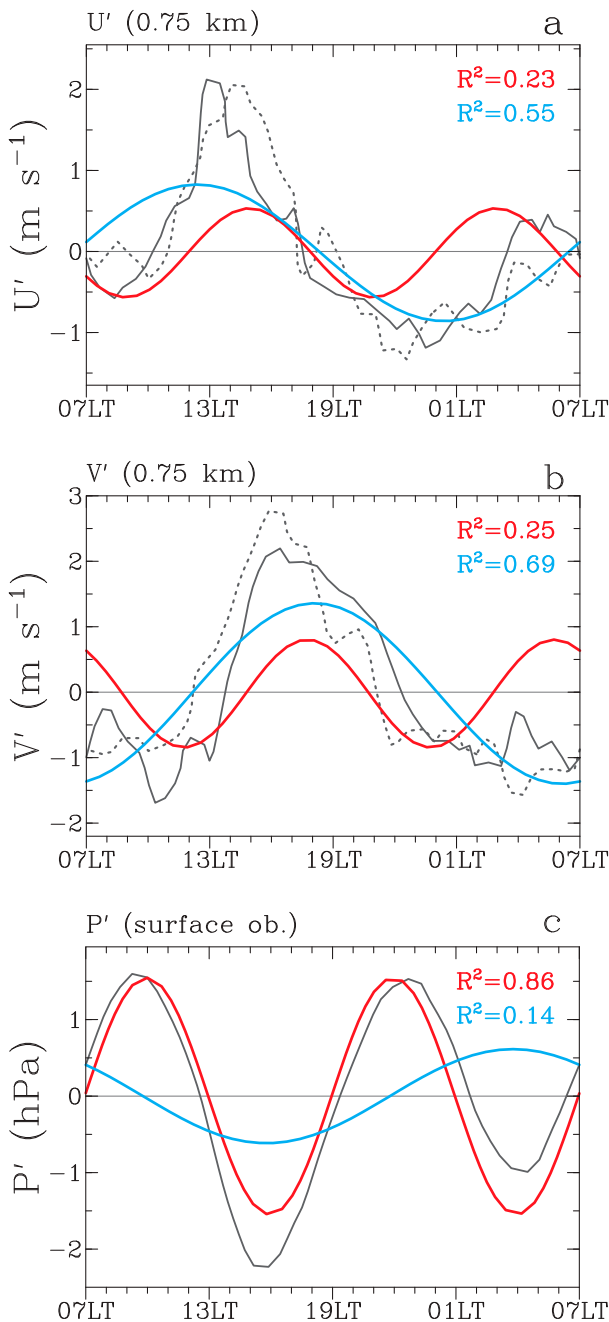


FIG. 3. (a) Time series of the daily cycle of zonal wind anomalies derived from the radar data and averaged over the radar domain at 0.75-km height (solid gray curve). The cyan and red curves represent the fitted diurnal and semidiurnal harmonics, respectively. The squared correlation coefficient of the harmonic analysis is denoted by R^2 . Time series of the daily cycle of surface zonal wind anomalies observed aboard the *Mirai* is superimposed by the dotted gray curve. (b) As in (a), but for meridional wind anomalies. (c) As in (a), but for sea level pressure anomalies observed aboard the *Mirai*.

semidiurnal pressure harmonic was 1.55 hPa at 1000/2200 LT, which was at least twice as high as that of its diurnal counterpart (0.61 hPa at 0400 LT). This result is consistent with the diurnal and semidiurnal variations in surface pressure observed in other tropical oceans (Dai and Wang 1999; Ueyama and Deser 2008). In addition, the maximum amplitudes and phases of the diurnal and semidiurnal pressure harmonics are congruent with the general global characteristics of the diurnal (~ 0.59 hPa and ~ 0512 LT) and semidiurnal (~ 1.16 hPa and $\sim 0945/2145$ LT) tidal surface pressure perturbations near the equator (Chapman and Lindzen 1970). In conjunction, the diurnal and semidiurnal harmonics explained 100% of the variance in the pressure. It appears that the diurnal and semidiurnal pressure oscillations observed in this study had global structures of migrating modes.

Previous studies have illustrated the characteristics of tidal wind oscillations forced by migrating tidal pressure gradients using a simple dynamic model (Carlson and Hastenrath 1970; Chapman and Lindzen 1970). According to Carlson and Hastenrath (1970), the diurnal and semidiurnal variations in zonal tidal wind are maximized when the respective tidal pressure oscillations reach their minimum values in both hemispheres. In addition, the phases of the diurnal and semidiurnal variations of the meridional tidal wind lead those of the respective tidal pressure waves by 6 and 3 h, respectively, in the Southern Hemisphere.

Comparing Figs. 3a and 3b with Fig. 3c shows that the diurnal harmonic of the zonal wind did not reach the maximum amplitude when the diurnal pressure harmonic was at a minimum, with a time difference of more than 3 h. In addition, the peak of the diurnal meridional wind harmonic led that of the diurnal pressure harmonic by more than 10 h, rather than by 6 h as predicted by the dynamic model. These results indicate that the phase of the diurnal wind field was distinct from that of the migrating tidal wind field. The inconsistency of the diurnal wind phase with the prediction from the tidal pressure gradient force suggests that the observed diurnal wind variation is locally driven, probably by the high and inhomogeneous mountains near the southwestern coast of Sumatra (Fig. 1), through processes such as those described by Bielli et al. (2002) and Muñoz (2008).

However, the phase relationship between the semidiurnal harmonics of the zonal and meridional winds and the semidiurnal pressure harmonic is consistent with that illustrated by the dynamic model. In fact, the peak times of the semidiurnal zonal (0300/1500 LT) and meridional (0600/1800 LT) winds (Figs. 3a,b) are very similar to those determined by Chapman and Lindzen (1970), who demonstrated that the zonal component of the semidiurnal tidal winds was maximized at 0344/1544 LT in both hemispheres, whereas their meridional component peaked at 0644/1844 LT in the Southern Hemisphere. The consistency of the semidiurnal wind phase with semidiurnal tidal oscillations implies that the semidiurnal wind variation is primarily associated with migrating tides.

The diurnal harmonic of the low-level divergence field (Fig. 4a) exhibited divergence and convergence that peaked during the day and night, respectively, which is consistent

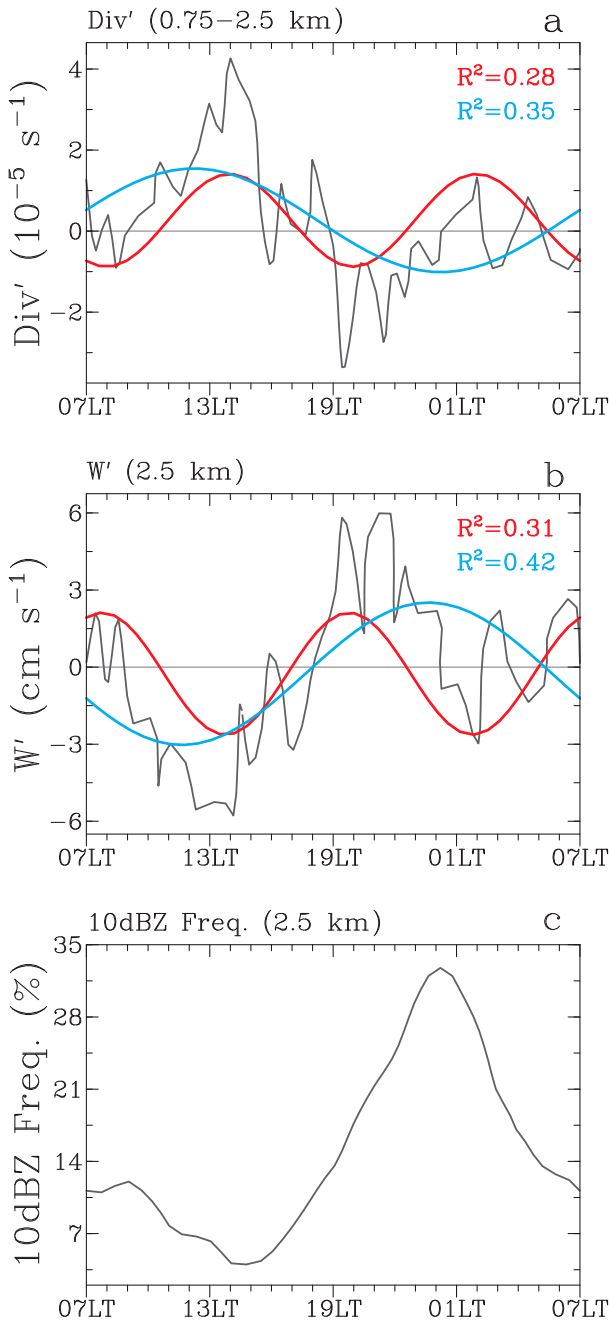


FIG. 4. (a) Time series of the daily cycle of divergence anomalies derived from the radar data and averaged over the radar domain at heights of 0.75–2.5 km. The cyan and red curves represent the fitted diurnal and semidiurnal harmonics, respectively. The squared correlation coefficient of the harmonic analysis is denoted by R^2 . (b) As in (a), but for vertical motion anomalies at 2.5-km height. (c) Time series of the daily cycle of occurrence frequency with reflectivity values of ≥ 10 dBZ averaged over the radar domain at 2.5-km height.

with the diurnal divergence cycle observed over the offshore regions of the Pacific and Atlantic Oceans (Dai and Deser 1999; Christophersen et al. 2020). Furthermore, a pronounced semidiurnal oscillation was observed in the divergence field.

The maximum amplitude of the diurnal divergence harmonic was $1.54 \times 10^{-5} \text{ s}^{-1}$, whereas that of its semidiurnal counterpart was $1.41 \times 10^{-5} \text{ s}^{-1}$. In addition, the diurnal and semidiurnal divergence harmonics explained 35% and 28% of the divergence variance, respectively. These results suggest a comparable contribution of diurnal and semidiurnal variations to the daily low-level divergence cycle, which is in contrast to the results of Dai and Deser (1999) that demonstrated the dominance of the diurnal cycle over the semidiurnal cycle for surface divergence.

Figure 4a shows that the total contribution of the diurnal and semidiurnal harmonics to the low-level (0.75–2.5 km) divergence variance was as high as 63%. The semidiurnal divergence harmonic showed a feature with its second peak (~ 1400 LT) and second trough (~ 2000 LT) of the day, nearly in phase with the peak and trough of the diurnal divergence harmonic, respectively. This indicates an approximate phase locking of the semidiurnal divergence variation to its diurnal counterpart. As a result, the strong divergence that occurred in the early afternoon (~ 1200 – 1500 LT) was coherent with the superimposition of the diurnal and semidiurnal divergence phases. In contrast, strong convergence was observed in the late evening and early night (~ 1900 – 2200 LT) when the convergence phases of diurnal and semidiurnal variations overlapped.

The diurnal harmonic of the vertical motion field was characterized by intense downdrafts around noon and intense updrafts before midnight (Fig. 4b). The maximum amplitude of the diurnal vertical motion harmonic (2.51 cm s^{-1}) was close to that of its semidiurnal counterpart (2.11 cm s^{-1}). In addition, the contributions of diurnal and semidiurnal harmonics (42% and 31%, respectively) to the vertical motion variance were comparable. These results imply comparable strengths for diurnal and semidiurnal vertical motion variations. Notably, diurnal and semidiurnal harmonics accounted for as much as 73% of the variance in the vertical motion. Corresponding to the daily cycle of the divergence field, strong downdrafts observed during the morning and afternoon were associated with the superimposition of diurnal and semidiurnal downdraft phases, whereas strong updrafts observed during the evening and night were related to the superimposition of diurnal and semidiurnal updraft phases (Figs. 4a,b). In addition, short-term (~ 1 – 3 -h) perturbations are evident in Figs. 4a and 4b.

Figure 4c shows the daily cycle of occurrence frequency with reflectivity values of ≥ 10 dBZ averaged over the radar domain at a 2.5-km height, which is used as a proxy for daily convective and precipitation activity. The highest 10-dBZ occurrence frequency occurred during the night around 0030 LT, consistent with previous studies relating to the nocturnal intensification of precipitation off the western and southwestern coasts of Sumatra (Mori et al. 2004; Wu et al. 2009; Yokoi et al. 2017; Geng et al. 2020). However, another smaller peak was observed in the 10-dBZ occurrence frequency at ~ 0900 LT, which corresponded well with the maximum semidiurnal updrafts (Figs. 4b,c).

Figure 4 shows that an increase in the 10-dBZ occurrence frequency is generally consistent with the enhancement of

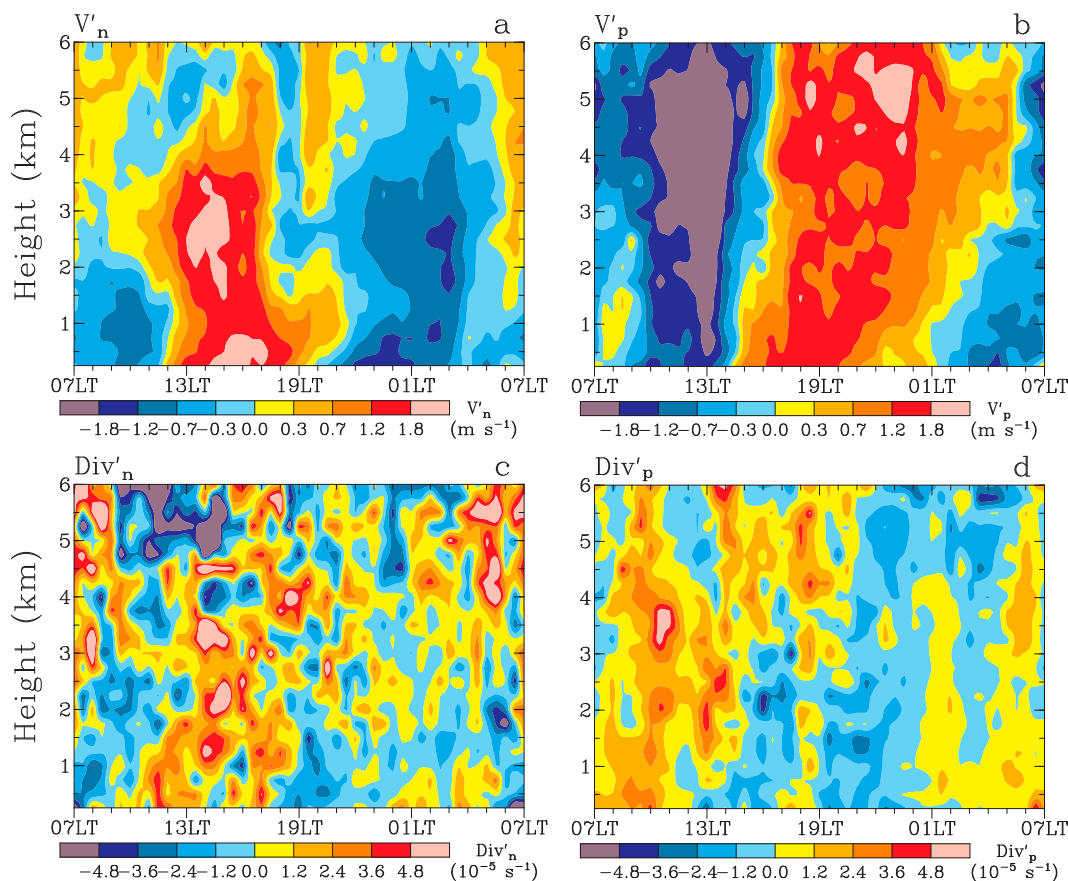


FIG. 5. (a) Time–height diagram of the daily cycle of cross-coast wind anomalies (color shades; m s^{-1}) derived from the radar data and averaged over the radar domain. The positive values correspond to the onshore winds, and the negative values indicate offshore winds. (b) As in (a), but for along-coast wind anomalies (color shades; m s^{-1}). The positive values denote the northwesterly, and the negative values represent southeasterly along-coast winds. (c) As in (a), but for divergence anomalies induced by the cross-coast wind (color shades; 10^{-5} s^{-1}). (d) As in (a), but for divergence anomalies induced by the along-coast wind (color shades; 10^{-5} s^{-1}).

the updrafts and low-level convergence. Both peaks of the 10-dBZ occurrence frequency formed $\sim 1\text{--}2$ h after the updrafts and low-level convergence were maximized. The highest peak of the 10-dBZ occurrence frequency around midnight corresponded well with the formation of strong convergence and updrafts owing to the superimposition of the diurnal and semidiurnal convergence and updraft phases. In contrast, the lowest value of the 10-dBZ occurrence frequency occurred around 1430 LT, when strong divergence and downdrafts were present, in association with the superimposition of the diurnal and semidiurnal divergence and downdraft phases. Furthermore, the secondary rainfall maximum around 0900 LT was weak, which can be attributed to the superimposition of the diurnal downdraft phase with the semidiurnal updraft phase. These results suggest that diurnal and semidiurnal wind variations play important roles in the development and suppression of convection through their induced updrafts and downdrafts, respectively.

Time–height diagrams of the daily cycle of the radar-derived cross- and along-coast kinematic variables are shown in Fig. 5.

The onshore (positive) wind dominated from late morning to early evening and shifted to an offshore (negative) wind at night (Fig. 5a). The diurnally varying cross-coast wind encompassed a height of up to ~ 5 km with a near-constant phase. In addition to diurnally varying cross-coast winds, onshore winds appeared around 0600–0700 LT, which were more pronounced at heights greater than 1.5 km. Furthermore, relatively intense offshore winds were observed in the low troposphere around 0800–1100 LT. These results indicate the existence of semidiurnal cross-coast wind variation.

There was also a significant diurnal variation in the along-coast wind (Fig. 5b). The positive along-coast wind (the northwesterly wind; see Fig. 1) was observed from the afternoon to the early night, while the negative one (the southeasterly wind) dominated from late night to morning hours. The diurnally varying along-coast wind extended from the surface to higher elevations, with a near-constant phase during most times of the day. A positive along-coast wind was also observed around 0700–0900 LT, which signifies a semidiurnal oscillation in the along-coast wind. Figures 5c and 5d show that

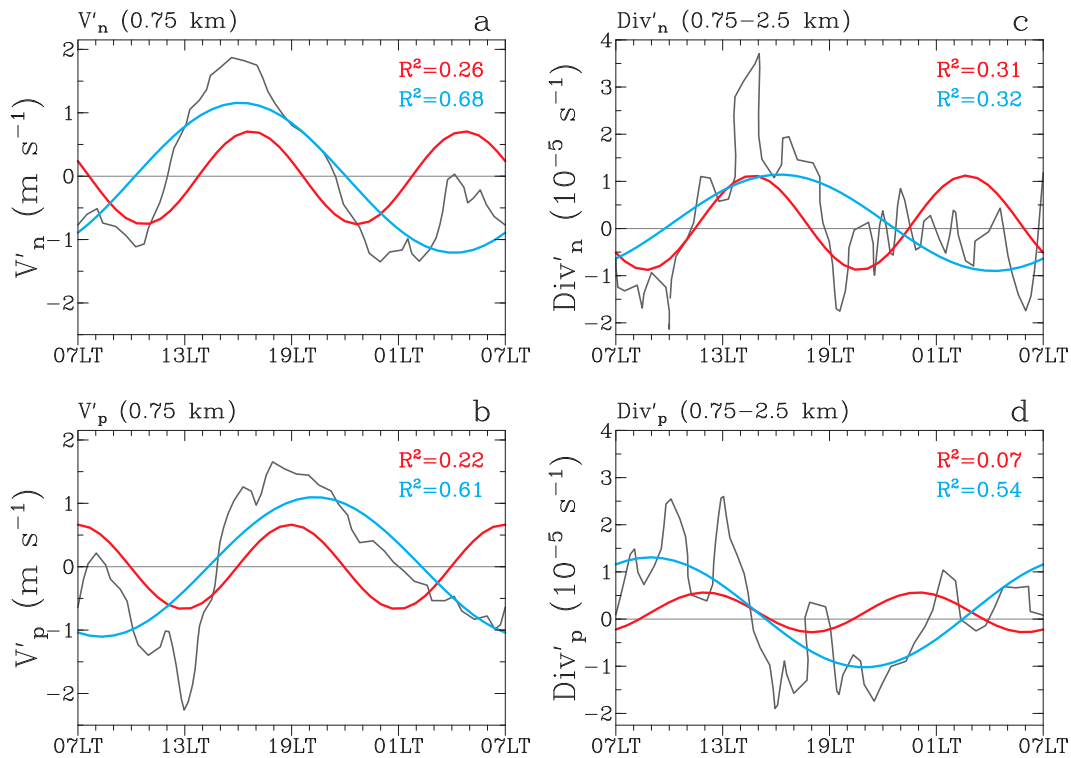


FIG. 6. (a) Time series of the daily cycle of cross-coast wind anomalies derived from the radar data and averaged over the radar domain at 0.75-km height (gray curve). The positive values correspond to the onshore winds, and the negative values indicate offshore winds. The cyan and red curves represent the fitted diurnal and semidiurnal harmonics, respectively. The squared correlation coefficient of the harmonic analysis is denoted by R^2 . (b) As in (a), but for along-coast wind anomalies. The positive values denote the northwestward, and the negative values represent southeastward along-coast winds. (c) As in (a), but for divergence anomalies induced by the cross-coast wind and averaged at heights of 0.75–2.5 km. (d) As in (a), but for divergence anomalies induced by the along-coast wind and averaged at heights of 0.75–2.5 km.

the divergence field was induced by both cross- and along-coast winds. The cross- and along-coast divergence fields also underwent diurnal and semidiurnal variations, as can be clearly seen in Fig. 6.

Figures 6a and 6b show that the maximum amplitudes of the diurnal and semidiurnal harmonics of the cross-coast wind were 1.16 and 0.76 m s^{-1} , respectively, while those of the along-coast wind were 1.1 and 0.66 m s^{-1} , respectively. This result implies that the strengths of the diurnal and semidiurnal variations in the along-coast wind were very close to those of the cross-coast wind. The diurnal and semidiurnal harmonics explained 68% and 26%, respectively, of the variance in the cross-coast wind, whereas they accounted for 61% and 22%, respectively, of the along-coast wind variance.

The approximate phase locking of the semidiurnal variation to the diurnal variation also occurred in both the cross-coast and along-coast winds. Figure 6a indicates that the intense onshore (positive) wind occurring from late afternoon to early evening (~ 1500 – 1800 LT) was consistent with the superimposition of the diurnal and semidiurnal onshore wind phases, whereas the intense offshore (negative) wind observed around midnight (~ 2300 – 0200 LT) was congruent with the superimposition of the diurnal and

semidiurnal offshore wind phases. For the along-coast wind, Fig. 6b indicates that the intense positive wind in the evening (~ 1700 – 2100 LT) and the intense negative wind in the late morning and early afternoon (~ 1100 – 1400 LT) were associated with the superimposition of the positive and negative wind phases, respectively, of the diurnal and semidiurnal harmonics.

Figures 6c and 6d show that the maximum diurnal amplitude of the cross-coast divergence field ($1.14 \times 10^{-5} \text{ s}^{-1}$) was close to that of its along-coast counterpart ($1.31 \times 10^{-5} \text{ s}^{-1}$), indicating that the diurnal strengths of the cross- and along-coast divergence fields are also comparable. On the other hand, the maximum amplitude of the semidiurnal harmonic of the cross-coast divergence field ($1.12 \times 10^{-5} \text{ s}^{-1}$) was almost twice as high as that of its along-coast counterpart ($0.57 \times 10^{-5} \text{ s}^{-1}$). The diurnal and semidiurnal harmonics explained 32% and 31% of the cross-coast divergence variance, respectively, indicating a comparable contribution of diurnal and semidiurnal variations in the cross-coast divergence field. In contrast, the contributions of diurnal and semidiurnal harmonics to the along-coast divergence variance were 54% and 7%, respectively (Fig. 6d), suggesting the dominance of diurnal variation over semidiurnal variation in the along-coast divergence field. In

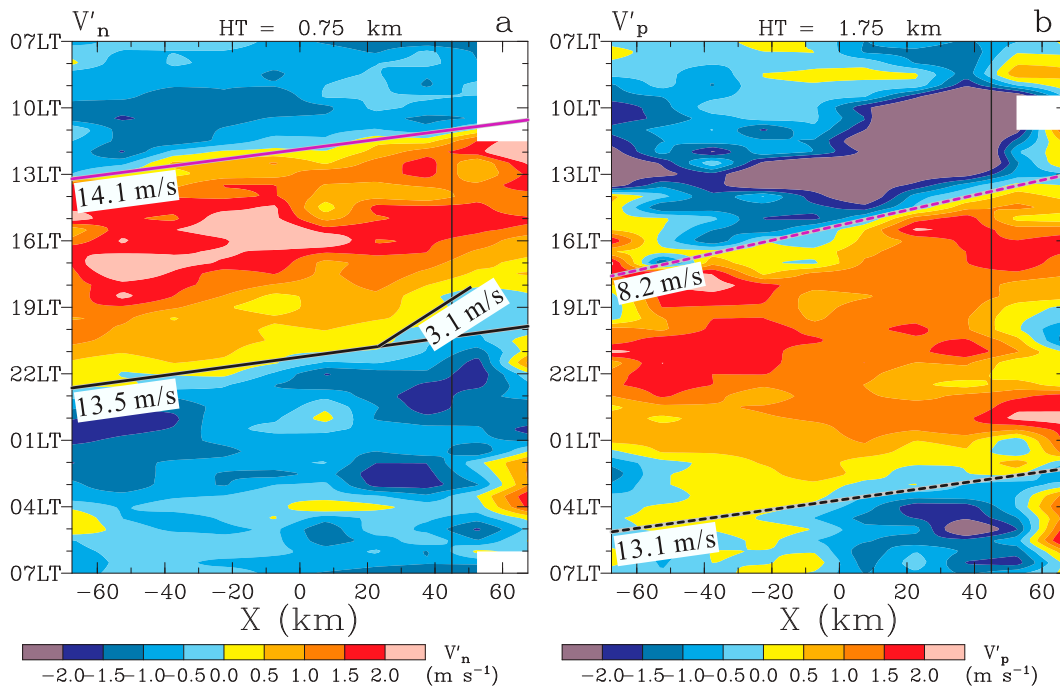


FIG. 7. (a) Time–distance section perpendicular to the coast of the daily cycle of cross-coast wind anomalies (color shades; m s^{-1}) derived from the radar data at 0.75-km height. The positive values correspond to the onshore winds, and the negative values indicate offshore winds. The vertical black line indicates the approximate location of the coast. The tilted solid purple and black lines outline the seaward propagations of the leading edges of onshore (positive) and offshore (negative) wind anomalies, respectively. (b) As in (a), but for along-coast wind anomalies (color shades; m s^{-1}) at 1.75-km height. The positive values denote the northwestward, and the negative values represent southeastward along-coast winds. The tilted dashed purple and black lines outline the seaward propagations of the leading edges of positive and negative along-coast wind anomalies, respectively.

addition to the diurnal and semidiurnal variations, the short-term ($\sim 1\text{--}3$ h) perturbations observed previously are also evident in Figs. 6c and 6d.

b. Daily offshore propagation of the wind field

Figure 7 shows time–distance sections perpendicular to the coast of the daily cycle of the cross- and along-coast winds. The trends of the relatively regular edges of the cross- and along-coast winds have been used to obtain information about the offshore propagation speeds of wind signals.

Figure 7a shows that at ~ 1100 LT, the winds near the coast started to become onshore (positive). As time progressed, the onshore wind underwent coherent seaward propagation from the coast and expanded out of the analysis domain (~ 112.5 km from the coast) by 1330 LT. The seaward propagation speed of the leading edge of the onshore wind envelope was ~ 14.1 m s^{-1} . The strong onshore wind propagating seaward from the coast in the afternoon and early evening was related to the superimposition of the diurnal and semidiurnal onshore wind phases (Fig. 6a). From ~ 1800 LT, the onshore wind near the coast was replaced by an offshore (negative) wind (Fig. 7a). The offshore wind around this time was relatively weak and propagated seaward at a low speed of ~ 3.1 m s^{-1} . The offshore wind intensified by 2100 LT, which was related to the superimposition of the diurnal and semidiurnal

offshore wind phases (Fig. 6a). The intensified offshore flow propagated seaward with a fast speed of ~ 13.5 m s^{-1} , overtaking the slow-propagating offshore flow around $x = 25$ km (~ 20 km from the coast) and propagating out of the analysis domain by 2230 LT (Fig. 7a).

As shown in Fig. 7b, the leading edge of the broad envelope of the positive along-coast wind began to propagate offshore from the coast at ~ 1400 LT, with a speed of ~ 8.2 m s^{-1} . By 1600 LT, a relatively strong and offshore-propagating positive along-coast wind appeared, which was associated with the superimposition of the positive along-coast wind phases of diurnal and semidiurnal variations (Fig. 6b). From ~ 0300 LT, the positive along-coast wind reversed to a negative wind near the coast (Fig. 7b). The negative along-coast wind then propagated offshore at a speed of ~ 13.1 m s^{-1} . Offshore propagation was also observed for the intense negative along-coast wind during the late morning and early afternoon, when the negative along-coast wind phases of the diurnal and semidiurnal variations overlapped (Fig. 6b). The along-coast wind also propagated out of the analysis domain (Fig. 7b).

As shown above, the wind field propagated offshore from the coast at various speeds, which is consistent with the results of previous studies on the offshore propagation of sea and land breezes (Gille et al. 2005; Brown et al. 2017; Kilpatrick

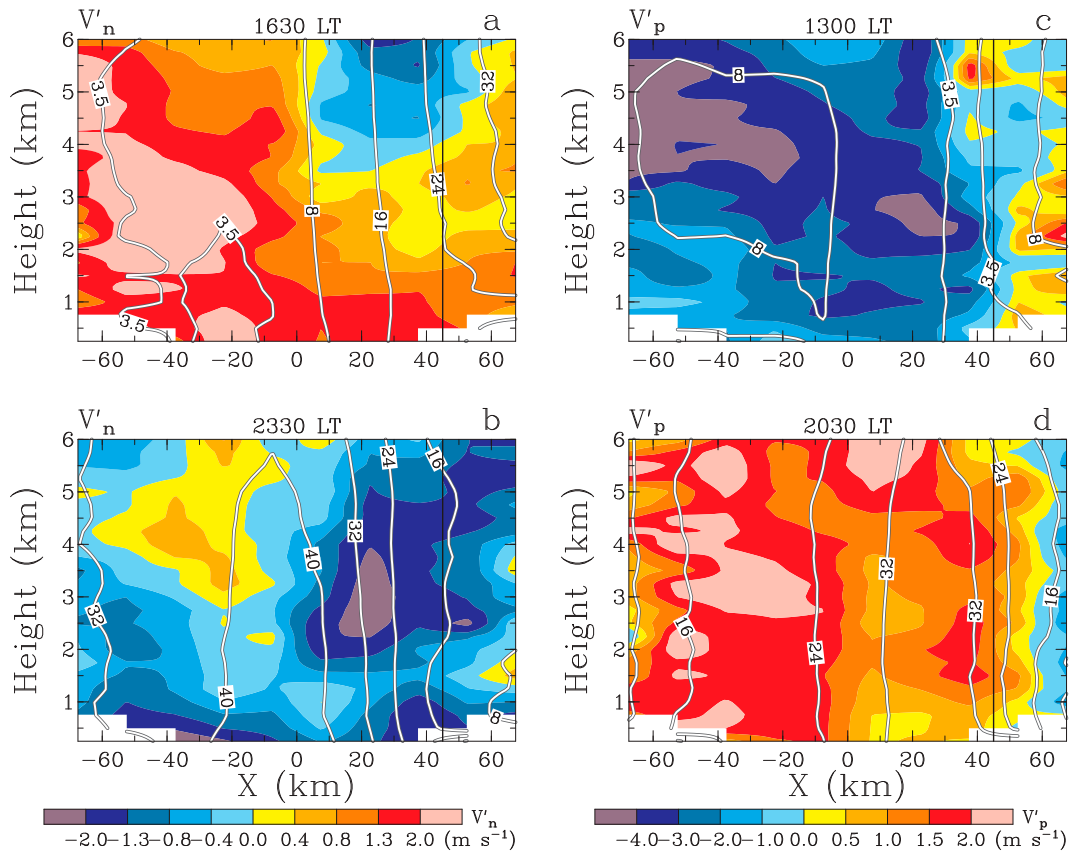


FIG. 8. (a),(b) Vertical cross sections perpendicular to the coast of cross-coast wind anomalies (color shades; m s^{-1}) and occurrence frequency with reflectivity values of ≥ 10 dBZ (white contours; %) derived from the radar data at (a) 1630 and (b) 2330 LT. For cross-coast wind anomalies, the positive values correspond to the onshore winds, and the negative values indicate offshore winds. The vertical black line indicates the approximate location of the coast. (c),(d) As in (a) and (b), but for along-coast wind anomalies (color shades; m s^{-1}) at (c) 1300 and (d) 2030 LT. The positive values denote the northwestward, and the negative values represent southeastward along-coast winds.

et al. 2017; Short et al. 2019). In this study, the slowest propagation speed found in the offshore wind (3.1 m s^{-1}) is consistent with the phase speed for a density current (Simpson 1969), while the other propagation speeds, ranging from 8.2 to 14.1 m s^{-1} , agree very well with those of gravity waves (Mapes et al. 2003; Tulich and Mapes 2008).

The occurrence of gravity waves is also reflected in Fig. 8, which shows a distinct tendency for both the cross- and along-coast winds to tilt upward with increasing distance from the coast. Such vertical features are consistent with the upward and outward ray paths of gravity waves generated by an overland heat source (Rotunno 1983). As shown by the distribution of the 10-dBZ occurrence frequency, these offshore propagating gravity waves were accompanied by either relatively strong (Figs. 8a,d) or weak (Figs. 8b,c) convection over land. This result indicates that the excitation of gravity waves may have been related to different thermal profiles in the troposphere, which explains the range of wave propagation speeds (Fig. 7) (Tulich and Mapes 2008). Following the methodology of Holton (2004), the phase speed of a gravity wave in a resting atmosphere can be represented by the equation

$c = N\lambda_z/2\pi$, where N represents the Brunt–Väisälä frequency and λ_z represents the vertical wavelength. Vertical profiles of anomalous potential temperature observed using radiosonde (Fig. 9a) indicated the presence of vertical wavelength structures ranging between 4.9 and 9.1 km. The mean value of N from the surface to 15 km is $\sim 0.01 \text{ s}^{-1}$ (not shown). Therefore, the radiosonde observations suggest the phase speeds of gravity waves between ~ 7.8 and 14.5 m s^{-1} , which are consistent with the wave propagation speeds derived from the radar data (Fig. 7).

Figure 8b shows the vertical feature when the fast-propagating offshore flow propagated ahead of the slow-propagating offshore flow (Fig. 7a). As shown in Fig. 8b, the fast-propagating offshore flow reached approximately $x = -65 \text{ km}$. The fast-propagating offshore flow was characterized by a seaward and upward tilt from approximately $x = -20 \text{ km}$ and from the surface to a height of $\sim 4 \text{ km}$, respectively, signifying its association with gravity waves (Rotunno 1983). The slow-propagating offshore flow possessed an elevated head of $\sim 1.5 \text{ km}$ deep near its leading edge (around $x = 10 \text{ km}$) and was concentrated in the lowest 1 km inland of the elevated

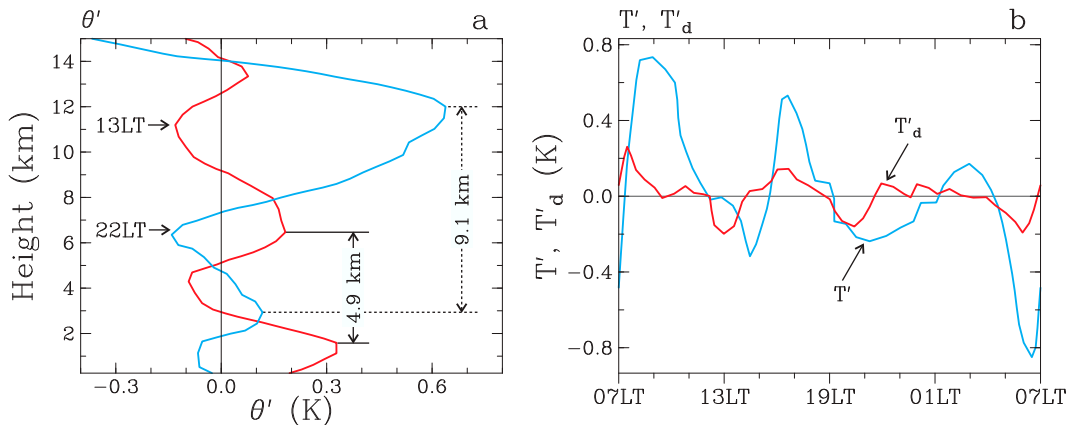


FIG. 9. (a) Vertical profiles of potential temperature anomalies, as derived from the radiosonde data at 1300 LT (red curve) and 2200 LT (cyan curve). (b) Time series of the daily cycle of surface temperature (cyan curve) and dewpoint temperature (red curve) anomalies observed at the Bengkulu meteorological station, with the diurnal and semidiurnal harmonics being removed from the data.

head. The vertical structure of the slow-propagating offshore flow is consistent with the density current (Simpson 1969). As it occurred considerably earlier than the typical formation of the land breeze after midnight (Hsu 1970; Houze et al. 1981; Case et al. 2005), the density current observed here may have been related to the katabatic flow induced by the mountains close to the southwestern coast of Sumatra (Figs. 1 and 7a) (Wu et al. 2009). Figure 9b shows the daily evolution of the surface temperature and dewpoint temperature observed at the Bengkulu meteorological station (Fig. 1), after removal of the diurnal and semidiurnal harmonics. Surface observations indicate that at ~ 1900 LT, there was a transition of temperature and dewpoint temperature anomalies from positive to negative, which is consistent with the density current observed by the *Mirai* radar at approximately this time (Fig. 7a).

c. Daily offshore propagation of the divergence field and precipitation

Figures 10a and 10b show the time–distance evolution of the vertical motion filed at 2.5 km as observed by the *Mirai* radar. During the analysis period, a series of updraft–downdraft couplets that occurred within an interval of several hours were observed daily. These updraft–downdraft couplets corresponded to a series of alternating convergent and divergent regions (not shown). Most of these updraft–downdraft couplets exhibited feature tilting from top right to bottom left, indicating that they primarily propagated from land to sea. The rapid alternation and seaward propagation of the updrafts and downdrafts were also evident in the daily analyses of the ERA5 data (Figs. 10c,d), confirming the observational results obtained from the *Mirai* radar. The perturbation pattern and seaward propagation of the vertical motion field illustrated in Fig. 10 provide evidence that short-time-scale gravity wave activity was significant on individual days during the analysis period.

Figures 11a shows the time–distance section perpendicular to the coast of the daily cycle of the low-level divergence field

observed by the *Mirai* radar. As shown in Fig. 4, the daily evolution of precipitation over the radar domain is closely related to the overall diurnal and semidiurnal evolution of the vertical motion and low-level divergence fields. However, Fig. 11a illustrates that the low-level divergence field also varies significantly over a time scale of $\sim 1\text{--}3$ h. A series of convergence–divergence couplets was observed, which propagated offshore along the previously illustrated gravity wave phase lines. A zone of intense convergence also propagated offshore and aligned with the density current. These results imply that short-term variation is closely related to offshore-propagating density currents or gravity waves.

Consistent with the short-term oscillations of the divergence field, a series of updraft–downdraft couplets propagated offshore along the gravity wave phase lines (Fig. 11b), indicative of further modulation of the gravity waves on the diurnally and semidiurnally varying wind fields.

An envelope of suppressed precipitation, as exemplified by the area with values of the 10-dBZ occurrence frequency $\leq 8\%$, occurred over the sea from 1100 to 2000 LT (Fig. 11). This corresponded to the suppression of convection due to divergence and downdrafts induced by semidiurnal and diurnal wind variations (Fig. 4). Figure 11 shows that the offshore propagation of the leading edge of the suppressed precipitation envelope is consistent with the offshore propagation of intense downdrafts and low-level divergence, approximately along the gravity wave phase line of 14.1 m s^{-1} . Furthermore, the minimum precipitation (3.5% 10-dBZ occurrence frequency) also propagated offshore, together with intense downdrafts and low-level divergence, approximately along the gravity wave phase line of 8.2 m s^{-1} . These results imply that gravity wave–induced downdrafts further helped to suppress daytime convection over the sea.

Further evidence of the suppression of convection over the sea due to gravity wave downdrafts is additionally visible in Figs. 12a and 12b. As shown in Figs. 12a and 12b, convection over the sea was inactive during the day, which was associated

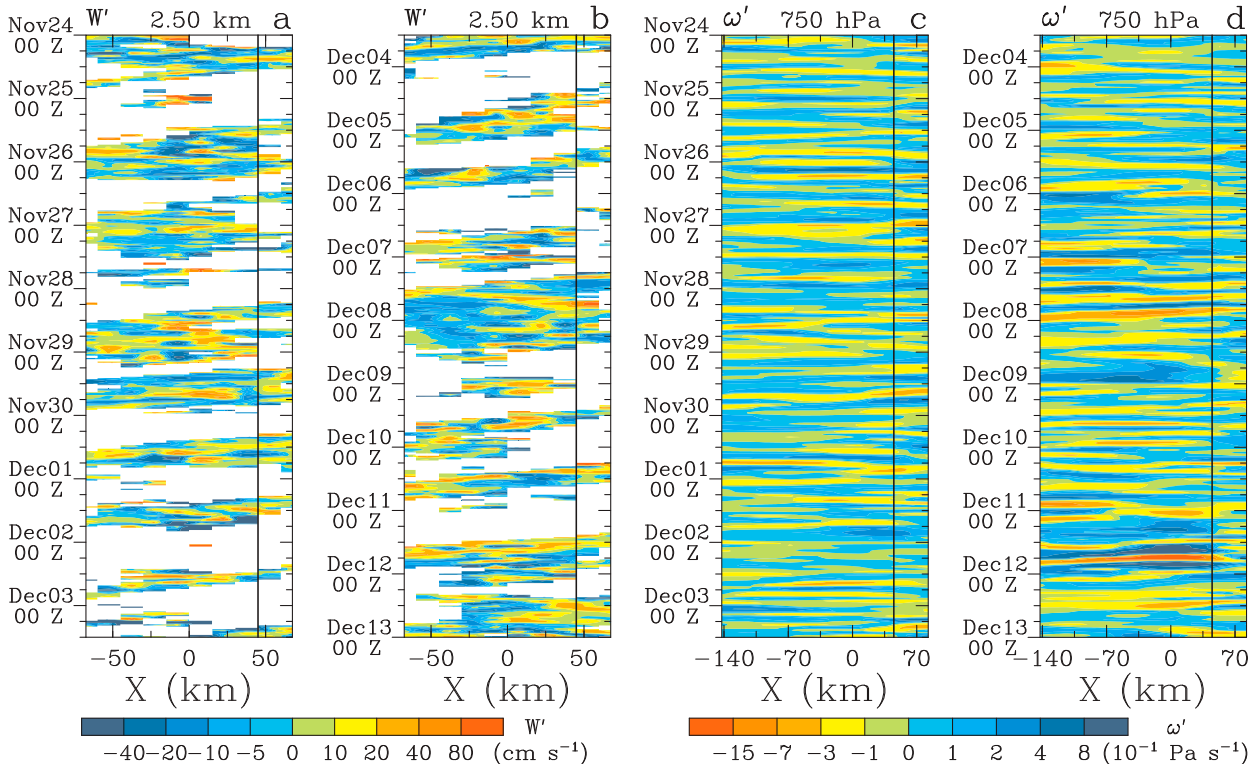


FIG. 10. (a),(b) Time–distance section perpendicular to the coast of vertical motion anomalies (color shades; cm s^{-1}) derived from the radar data at 2.5-km height during 24 Nov–13 Dec 2015. (c),(d) Time–distance section perpendicular to the coast of vertical- p motion anomalies (color shades; $10^{-1} \text{ Pa s}^{-1}$) at 750 hPa, derived from the ERA5 data along the cyan line shown in Fig. 1b, with the diurnal and semidiurnal harmonics being removed from the data. In (c) and (d), the cold and warm colors denote positive (downdraft) and negative (updraft) anomalies, respectively. The vertical black line in each panel indicates the approximate location of the coast.

with the superimposition of the divergence and downdraft phases of diurnal and semidiurnal wind variations (Fig. 4). Figures 12a and 12b indicate the existence of oscillations both in the cross-coast wind and in the vertical motion field. Such oscillations are a signature of gravity waves. Based on the vertical motion, the horizontal wavelength of the gravity wave was approximately 50–60 km. Figure 13a indicates the existence of oscillations between 1400 and 1600 LT daily. The downdrafts peaks were generally observed around $x = 0$ km and between $x = 30$ and 67 km, which is consistent with the result observed in the mean daily cycle (Fig. 12b). Furthermore, Figs. 13b–d indicate that each of these downdraft peaks exhibited a seaward propagation on individual days. The results illustrated in Fig. 13 reinforce the signature of gravity waves revealed in the mean daily cycle (Fig. 12b).

Figure 12b indicates that the gravity wave was characterized by a stronger downdraft than the updraft, which is in good agreement with the superimposition of the gravity wave–induced vertical motions on the diurnal and semidiurnal downdrafts. Between $x = -20$ and 20 km, intense gravity wave–assisted downdrafts penetrated downward from the middle to the lower troposphere. A region of minimum precipitation, as indicated by the area with values of the 10-dBZ occurrence frequency $\leq 3.5\%$, was observed between $x = -5$ and 20 km (25–50 km from the coast). The offshore minimum

precipitation was found to be collocated with deep and intense downdrafts aided by gravity waves, which demonstrates the effect of gravity wave downdrafts on further inhibiting rainfall over the sea. This is likely due to the increase in static stability and drying caused by gravity wave downdrafts (Liu and Moncrieff 2004; Lane and Zhang 2011).

Returning to Fig. 11, it is apparent that a broad envelope of precipitation, as exemplified by the region with values of the 10-dBZ occurrence frequency $\geq 16\%$, existed over the sea from ~ 1600 to 0500 LT, which was associated with semidiurnally and diurnally forced convergence and updrafts (Fig. 4). Generally, the leading edge of the precipitation envelope propagated offshore with updrafts and low-level convergence (Fig. 11). The offshore propagation speed of the leading edge of the precipitation envelope identified by the 10-dBZ occurrence frequency was $\sim 7.1 \text{ m s}^{-1}$ (not shown), which is close to the offshore propagation speed (8 m s^{-1}) of the rain-rate envelope observed during the Pre-YMC period (Yokoi et al. 2017).

The onset of intense precipitation over the sea, such as the region with values of the 10-dBZ occurrence frequency $\geq 32\%$, occurred within the precipitation envelope after 1800 LT (Fig. 11), which corresponds well with the diurnal and semidiurnal intensification of updrafts and low-level convergence (Fig. 4), as well as the diurnal and semidiurnal transition from

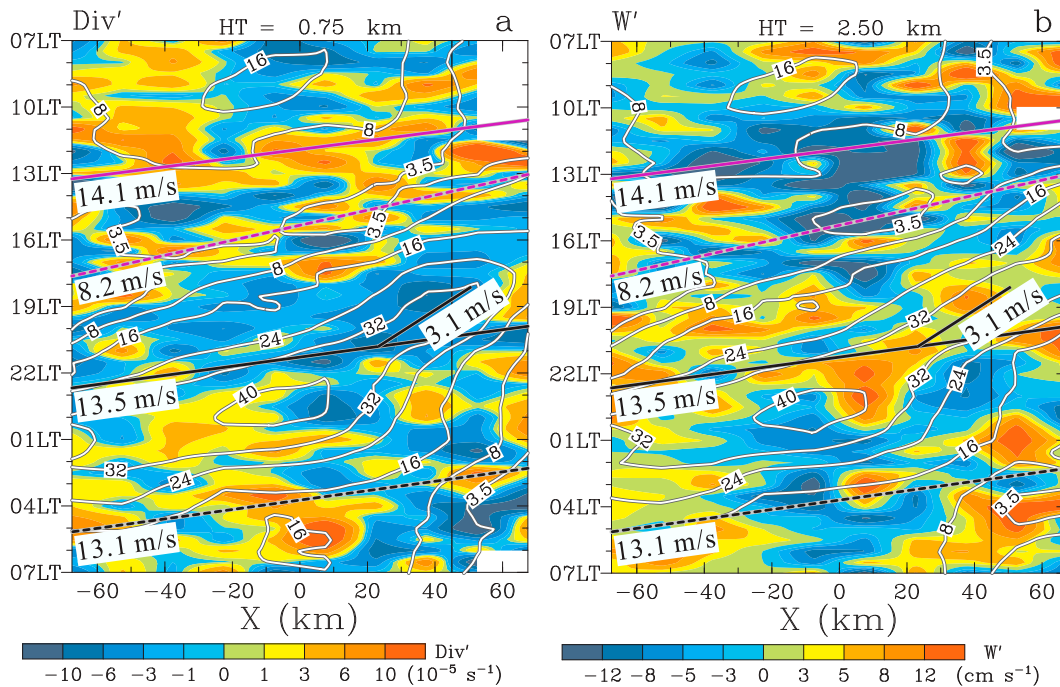


FIG. 11. (a) Time–distance section perpendicular to the coast of the daily cycle of divergence anomalies (color shades; 10^{-5} s^{-1}) and occurrence frequency with reflectivity values of ≥ 10 dBZ (white contours; %) derived from the radar data at 0.75-km height. The vertical black line indicates the approximate location of the coast. The tilted solid purple and black lines outline the seaward propagations of the leading edges of onshore and offshore wind anomalies, respectively, as shown in Fig. 7a. The tilted dashed purple and black lines outline the seaward propagations of the leading edges of positive and negative along-coast wind anomalies, respectively, as shown in Fig. 7b. (b) As in (a), but for vertical motion anomalies (color shades; cm s^{-1}) and occurrence frequency with reflectivity values of ≥ 10 dBZ (white contours; %) at 2.5-km height.

the onshore flow to the offshore flow (Fig. 6a). In addition, intense offshore precipitation was associated with the offshore propagation of density currents and gravity waves (Fig. 7a). We observed that in addition to the semidiurnal and diurnal forcings, the development of nocturnal intense precipitation over the sea was further assisted by the density current and/or gravity waves in three aspects.

First, intense offshore precipitation emerged near the coast together with the density current and propagated offshore in phase with the density current at a slow speed of $\sim 3.1 \text{ m s}^{-1}$ (Fig. 11). The slow propagation speed near the coast of the intense precipitation as judged from the 10-dBZ occurrence frequency is consistent with Yokoi et al. (2017), who found a propagation speed of 3.3 m s^{-1} for intense rain rate near the coast during the Pre-YMC period. The intense offshore precipitation near the coast was associated with intense updrafts and low-level convergence aligned with the path of the density current (Figs. 7a and 11). This can be attributed to the collision of the density current with the low-level onshore flow forming over the sea at earlier times of the day. Evidently, the density current converging with the previously formed onshore flow contributed to the enhancement of precipitation and slow offshore propagation of intense precipitation near the coast.

Second, the heaviest precipitation (e.g., the region of $\geq 40\%$ 10-dBZ occurrence frequency) occurred between $x = -30$ and

10 km (35–75 km away from the coast) around 2230–0030 LT (Fig. 11). This is consistent with previous studies on the occurrence of the heaviest precipitation off the western and southwestern coasts of Sumatra around midnight (Mori et al. 2004; Wu et al. 2009; Yokoi et al. 2017; Geng et al. 2020). The heaviest offshore precipitation in this study was observed after the leading edge of the rising phase of the gravity wave along the phase line of 13.5 m s^{-1} overtook the leading edge of the density current (Fig. 11b). Compared with the density current, stronger updrafts were formed with the coupling between the gravity wave updrafts and density current lifting. Consequently, the cooperation of density current lifting and gravity wave updrafts assisted in the development of the heaviest precipitation over the sea.

Finally, after the gravity wave propagated well ahead of the density current, intense precipitation far from the coast occurred with the arrival of the rising phase of the gravity wave (Fig. 11b). Thereafter, the offshore propagation of intense precipitation accelerated, reaching a speed similar to that of the gravity wave ($\sim 13.5 \text{ m s}^{-1}$). These patterns indicate that gravity wave updrafts also contributed to the enhancement of precipitation and the propagation of intense precipitation far from the coast.

Figures 12c and 12d further highlight the nighttime enhancement of convection over the sea through the cooperative

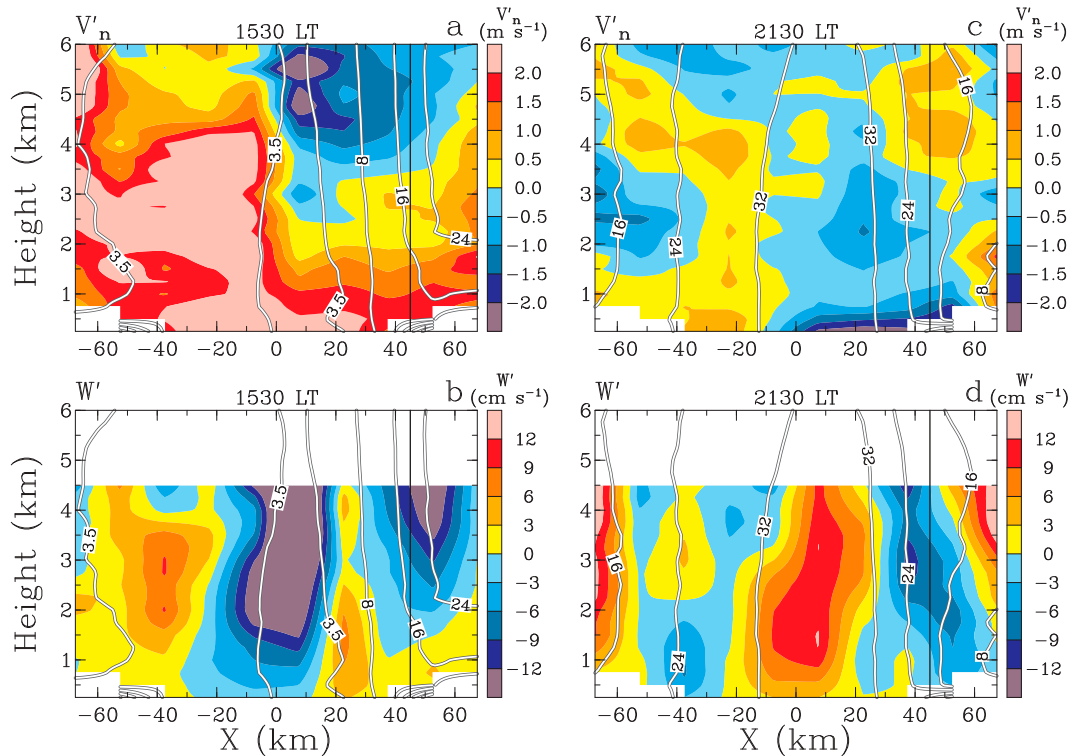


FIG. 12. (a),(b) Vertical cross sections perpendicular to the coast of (a) cross-coast wind anomalies (color shades; $m s^{-1}$) and (b) vertical motion anomalies (color shades; $cm s^{-1}$) derived from the radar data at 1530 LT. For cross-coast wind anomalies, the positive values correspond to the onshore winds, and the negative values indicate offshore winds. The vertical distribution of occurrence frequency with reflectivity values of ≥ 10 dBZ (white contours; %) is superimposed in each figure. The vertical black line indicates the approximate location of the coast. (c),(d) As in (a) and (b), but for 2130 LT.

effect of density current lifting and gravity wave updrafts. As shown in Figs. 12c and 12d, offshore convection was active in relation to the superimposition of diurnally and semidiurnally forced convergence and updrafts (Fig. 4). The gravity wave manifested itself as a series of onshore-offshore-flow and updraft-downdraft couplets (Figs. 12c,d). Generally, the gravity wave demonstrated a stronger updraft than the downdraft, which is consistent with the evolution of the gravity wave under diurnal and semidiurnal updraft conditions.

The density current manifested as intense offshore flow concentrated below a height of 1 km (Fig. 12c). Collision of the density current with the onshore flow was clearly observed around $x = -10$ km, with gravity wave updrafts hanging over the leading edge of the density current (Figs. 12c,d). Accompanying the vertical coupling of the density current lifting and wave updrafts aloft, intense updrafts formed and extended from the surface to high elevations, which were properly collocated with a heavy and deep precipitation region over the sea between $x = -10$ and 30 km (15–75 km from the coast). Therefore, these results indicate that the combined effects of the density current and gravity wave updrafts lead to further enhancement of deep convection over the sea, which is consistent with results of previous studies on the convective development triggered by the interaction of density currents and

gravity waves (Stensrud and Fritsch 1993; Anabor et al. 2009). Similar to the process described in Su and Zhai (2017), the coupling of density current-induced convergence and gravity wave updrafts can intensify the low-level lifting, thereby strengthening convection.

Figure 14a shows the time–distance section perpendicular to the coast of the daily cycle of the vertical motion field derived from the ERA5 data at 750 hPa. Similar to radar observations, ERA5 displays pronounced diurnal and semidiurnal variations. Relatively weak upward motions around 0800–1100 LT and strong upward motions around 1900–0400 LT corresponded well with the weak and strong daily rainfall peaks, respectively, which is in good agreement with what was observed by the *Mirai* radar (Figs. 4b,c). Figure 14a also exhibits the superimposition of short-time-scale and offshore-propagating gravity wave–like disturbances on diurnal and semidiurnal variations. This is more evident in Fig. 14b, where the diurnal and semidiurnal harmonics were removed. Figure 14b indicates that offshore-propagating gravity waves displayed a dominant period of ~ 2 –4 h and propagation speeds ranging from ~ 11.1 to $30.4 m s^{-1}$. Therefore, except for a much faster propagation speed of $\sim 30.4 m s^{-1}$, the ERA5-derived period and offshore propagation of gravity waves were in good agreement with those observed by the *Mirai* radar (Fig. 11).

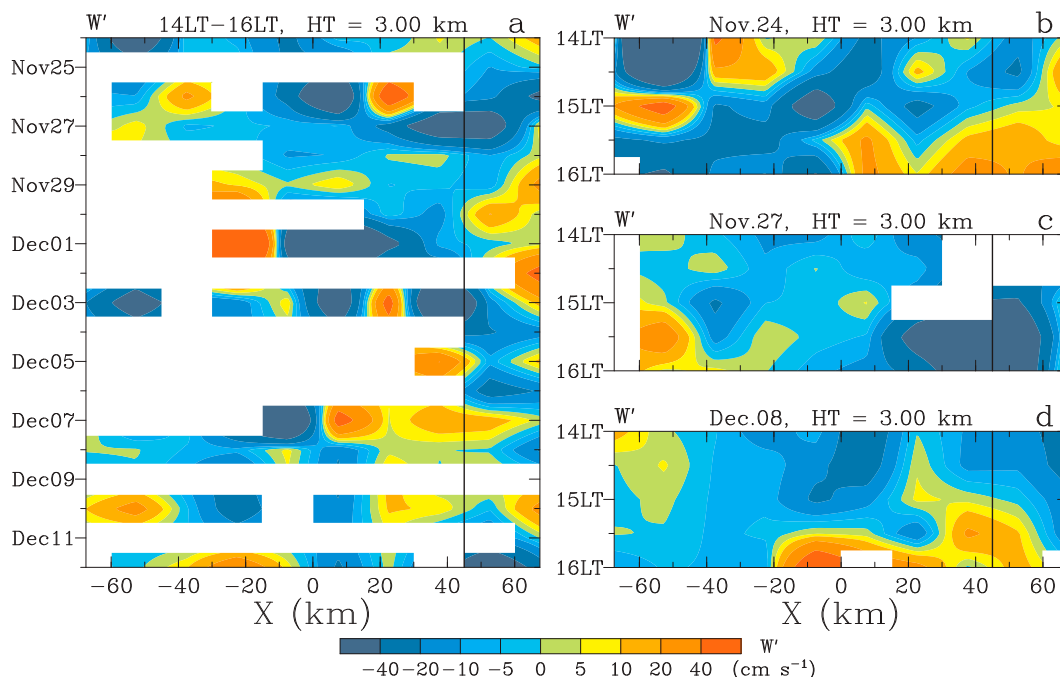


FIG. 13. (a) Time–distance section perpendicular to the coast of vertical motion anomalies (color shades; cm s^{-1}) derived from the radar data at 3-km height and averaged between 1400 and 1600 LT daily from 24 Nov to 12 Dec 2015. (b)–(d) A closer look at the time–distance section perpendicular to the coast of vertical motion anomalies for 24 Nov, 27 Nov, and 8 Dec 2015, respectively. The vertical black line in each panel indicates the approximate location of the coast.

The major discrepancy between the ERA5 and radar observation is that the former displays horizontal wavelength of gravity waves ranging from ~ 150 to 400 km (Fig. 14b), which is longer than the horizontal wavelength of ~ 50 – 60 km, as observed by the *Mirai* radar (Fig. 12). This discrepancy is possibly due to the coarse horizontal resolution (0.25° latitude–longitude grid space) of the ERA5 data. Nevertheless, despite this discrepancy, the results of ERA5 further support the radar-captured signatures of the daily wind cycle off the southwestern coast of Sumatra, including diurnal, semidiurnal, and short-term variations.

4. Summary and discussion

a. Summary

The daily cycle of the wind and divergence fields observed off the southwestern coast of Sumatra during the Pre-YMC period was investigated using single-Doppler radar data. The radar data were collected aboard the Research Vessel *Mirai* from 24 November to 13 December 2015, when both the wind field and precipitation underwent a pronounced daily variation. An algorithm was developed to retrieve the wind and divergence fields from the single-Doppler data. The daily cycle of each kinematic variable was further obtained by averaging the departures from the period mean at individual local times.

The observed daily cycles of the wind and divergence fields consisted of diurnal, semidiurnal, and short-term variations. The main characteristics of each temporal variation are as follows.

- 1) The phase of the diurnal wind variation was inconsistent with the predictions from the tidal pressure gradient force. The diurnal variations in the cross-coast wind, along-coast wind, and vertical motion field exhibited a near-constant phase in the low and middle troposphere. The strengths of the along-coast wind and its induced divergence field were comparable to those of their cross-coast counterparts.
- 2) The phase of the semidiurnal wind variation was consistent with the semidiurnal tidal oscillations. The semidiurnal vertical motion and low-level divergence fields demonstrated strengths comparable to those of their diurnal counterparts. There was an approximate phase locking of the semidiurnal variation with the diurnal variation in the wind and divergence fields.
- 3) Short-term wind variation is associated with density currents or gravity waves propagating offshore. The gravity waves displayed horizontal wavelengths of ~ 50 – 60 km and periods of ~ 1 – 3 h.
- 4) The diurnal and semidiurnal vertical motion variations resulting from the corresponding variations in the low-level divergence field contributed up to 73% of the daily vertical motion variance. The precipitation propagated offshore, in phase with the density current and gravity waves. There was further association of the diurnally and semidiurnally forced intense nighttime and weak daytime precipitation with the lifting effect of the density current and/or gravity waves and gravity wave downdrafts, respectively.

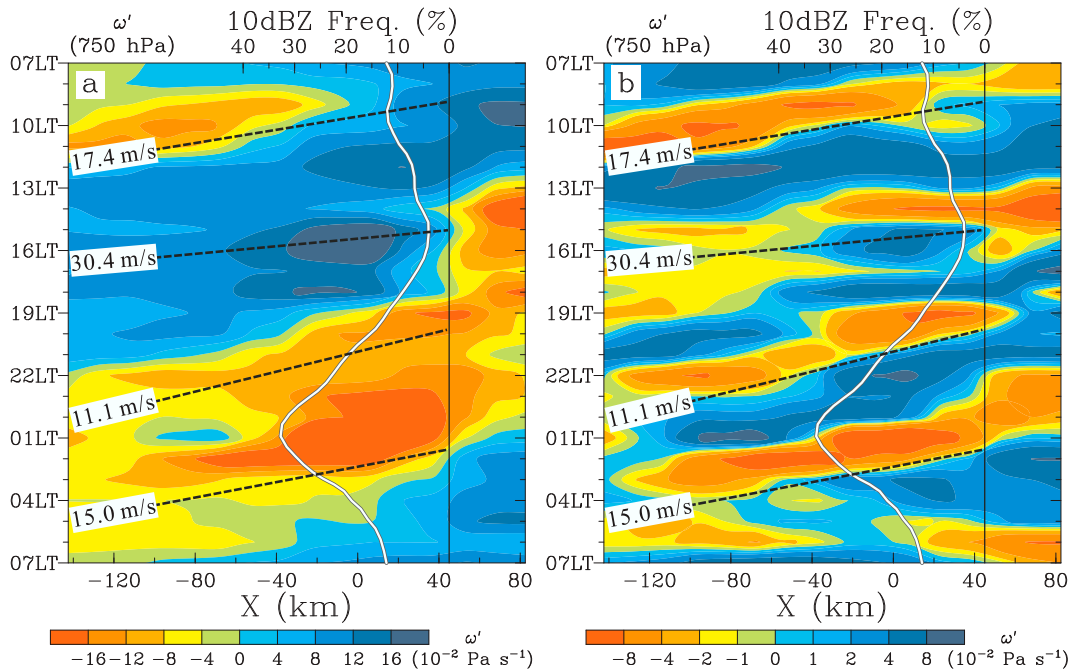


FIG. 14. (a) Time–distance section perpendicular to the coast of the daily cycle of vertical- p motion anomalies (color shades; 10^{-2} Pa s^{-1}) at 750 hPa, derived from the ERA5 data along the cyan line shown in Fig. 1b. The white curve represents the time series of the daily cycle of occurrence frequency with reflectivity values of ≥ 10 dBZ derived from the radar data and averaged over the radar domain at 2.5-km height. The vertical black line indicates the approximate location of the coast. The tilted dashed black line outlines the seaward propagation of vertical motion anomalies. The cold and warm colors denote positive (downdraft) and negative (updraft) anomalies, respectively. (b) As in (a), but with the diurnal and semidiurnal harmonics being removed.

b. Discussion

The results of this study suggest that locally driven diurnal circulation is fundamentally deep and three-dimensional off the southwestern coast of Sumatra, in contrast with the low-troposphere sea–land breeze circulation emphasized in previous studies (Mori et al. 2004; Wei et al. 2020; Bai et al. 2021). The along-coast wind off the southwestern coast of Sumatra has rarely been investigated. Our study revealed for the first time that the diurnal variability of the along-coast wind can be as significant as that of the cross-coast wind and may not be negligible in this region.

The results of this study further suggest, for the first time, that semidiurnal wind variation due to the migrating tidal effect plays a role comparable to its diurnal counterpart in forcing convection and rainfall off the southwestern coast of Sumatra. Specifically, the approximate phase locking of the semidiurnal wind and divergence variations to their diurnal counterparts manifests the reinforcement of diurnal wind variation by its semidiurnal counterpart. Consequently, our results emphasize the importance of semidiurnal wind variation in modulating daily kinematic structure and precipitation off the southwestern coast of Sumatra.

Because of their horizontal wavelengths of ~ 50 – 60 km and periods of ~ 1 – 3 h, the observed gravity waves are fundamentally mesoscale in character (Uccellini and Koch 1987; Koch and O’Handley 1997). This result is in contrast to the diurnal gravity waves illustrated in previous studies on the western

and southwestern coasts of Sumatra (Mori et al. 2004; Love et al. 2011; Yokoi et al. 2017; Wei et al. 2020; Bai et al. 2021). Yokoi et al. (2017) noted the importance of diurnal gravity waves in the diurnal precipitation cycle observed during the Pre-YMC period. However, their recognition of gravity waves was primarily based on the data from radiosondes launched every 3 h. The coarse temporal resolution of the radiosonde data may have hindered the detection of mesoscale gravity waves during the Pre-YMC period. This suggests that high-temporal-resolution data, such as the Doppler radar data used in this study (i.e., 6-min resolution), are necessary to accurately identify the daily wind cycle.

The high contribution (up to 73%) of diurnal and semidiurnal vertical motion variations to the daily vertical motion variance emphasizes that these wind variations exert a dominant effect on the daily precipitation cycle, while the density current and gravity waves are only of secondary importance. Furthermore, the daily analyses of the ERA5 data indicate that the impact of diurnal and semidiurnal vertical motion variations on the vertical motion variance during the analysis period was also higher than that of the short-term variations on each day, with exceptions for 26 November and 9 December when both diurnal and semidiurnal variations were extremely weak (not shown). Weak diurnal variations could be due to the large-scale suppression of convection during the Pre-YMC period (Geng et al. 2020). Therefore, the results of this study are in contrast with those of previous studies (Mori et al. 2004; Wu

et al. 2009; Love et al. 2011; Yokoi et al. 2017; Wei et al. 2020; Bai et al. 2021), where the density current (such as the land breeze or terrain-induced katabatic flow) or gravity waves played a crucial role in the development of diurnal precipitation off the western and southwestern coasts of Sumatra. Nevertheless, the movement of precipitation in phase with the density current and gravity waves implies that they can exert a controlling influence on the offshore propagation of daily precipitation, which is consistent with previous studies.

Our results highlight the multiple-time-scale wind variabilities of less than a day in modulating the daily precipitation cycle off the southwestern coast of Sumatra. It appears that the superimposition of the updrafts induced by the density current and mesoscale gravity waves with the intense updrafts induced by diurnal and semidiurnal variations in the low-level divergence field provides the most favorable conditions for the development of strong nocturnal precipitation frequently observed off the southwestern coast of Sumatra.

The data analyzed in this study cover a period of only 19 days, just before the passage of the intensive convective activity associated with a boreal winter MJO event. Although the results presented in this study shed some light on the daily and subdaily wind variations off the southwestern coast of Sumatra, it is necessary to investigate data over a significantly longer period and larger area to build a more robust understanding of the daily wind cycle around the Maritime Continent. We observed that the daily convective signatures captured by the high-temporal-resolution ERA5 data during the analysis period (Figs. 10c,d and 14) were consistent with those observed by the *Mirai* radar. Therefore, in future studies, more comprehensive field campaigns and long-term ERA5 data will be useful to reveal the similarities and differences of the daily wind cycle, either between various stages of the MJO, between distinct large-scale disturbances, or between different locations of the Maritime Continent.

Acknowledgments. We are grateful to all crew members of the Research Vessel *Mirai* and the technical staff of Global Ocean Development Inc. for their support in field operations during the Pre-YMC campaign. We also thank the peer reviewers for their thorough review and valuable suggestions, which were of great help in improving the manuscript.

Data availability statement. The data collected during the Pre-YMC campaign are available at https://www.jamstec.go.jp/ymc/obs/obs_preYMC.html.

REFERENCES

- Anabor, V., D. J. Stensrud, and O. L. L. de Moraes, 2009: Simulation of a serial upstream-propagating mesoscale convective system event over southeastern South America using composite initial conditions. *Mon. Wea. Rev.*, **137**, 2144–2163, <https://doi.org/10.1175/2008MWR2617.1>.
- Armijo, L., 1969: A theory for the determination of wind and precipitation velocities with Doppler radars. *J. Atmos. Sci.*, **26**, 570–573, [https://doi.org/10.1175/1520-0469\(1969\)026<0570:ATFTDO>2.0.CO;2](https://doi.org/10.1175/1520-0469(1969)026<0570:ATFTDO>2.0.CO;2).
- Bai, H., and Coauthors, 2021: Formation of nocturnal offshore rainfall near the west coast of Sumatra: Land breeze or gravity wave? *Mon. Wea. Rev.*, **149**, 715–731, <https://doi.org/10.1175/MWR-D-20-0179.1>.
- Bielli, S., P. Barbour, R. Samelson, E. Skillingstad, and J. Wilczak, 2002: Study of the diurnal cycle along the central Oregon coast during summertime northerly flow. *Mon. Wea. Rev.*, **130**, 992–1008, [https://doi.org/10.1175/1520-0493\(2002\)130<0992:NSOTDC>2.0.CO;2](https://doi.org/10.1175/1520-0493(2002)130<0992:NSOTDC>2.0.CO;2).
- Brier, G. W., and J. Simpson, 1969: Tropical cloudiness and rainfall related to pressure and tidal variations. *Quart. J. Roy. Meteor. Soc.*, **95**, 120–147, <https://doi.org/10.1002/qj.49709540309>.
- Brown, A. L., C. L. Vincent, T. P. Lane, E. Short, and H. Nguyen, 2017: Scatterometer estimates of the tropical sea-breeze circulation near Darwin, with comparison to regional models. *Quart. J. Roy. Meteor. Soc.*, **143**, 2818–2831, <https://doi.org/10.1002/qj.3131>.
- Carlson, G. C., Jr., and S. Hastenrath, 1970: Diurnal variation of wind, pressure, and temperature in the troposphere and stratosphere over Eniwetok. *Mon. Wea. Rev.*, **98**, 408–416, [https://doi.org/10.1175/1520-0493\(1970\)098<0408:DVOWPA>2.3.CO;2](https://doi.org/10.1175/1520-0493(1970)098<0408:DVOWPA>2.3.CO;2).
- Case, J. L., M. M. Wheeler, J. Manobianco, J. W. Weems, and W. P. Roeder, 2005: A 7-yr climatological study of land breezes over the Florida spaceport. *J. Appl. Meteor.*, **44**, 340–356, <https://doi.org/10.1175/JAM-2202.1>.
- Chapman, S., and R. S. Lindzen, 1970: *Atmospheric Tides: Thermal and Gravitational*. Gordon and Breach, 200 pp.
- Christoffersen, J. A., G. R. Foltz, and R. C. Perez, 2020: Surface expressions of atmospheric thermal tides in the tropical Atlantic and their impact on open-ocean precipitation. *J. Geophys. Res. Atmos.*, **125**, e2019JD031997, <https://doi.org/10.1029/2019JD031997>.
- Cotton, W. R., and R. A. Anthes, 1989: *Storm and Cloud Dynamics*. Academic Press, 883 pp.
- Dai, A., 2001: Global precipitation and thunderstorm frequencies. Part II: Diurnal variations. *J. Climate*, **14**, 1112–1128, [https://doi.org/10.1175/1520-0442\(2001\)014<1112:GPATFP>2.0.CO;2](https://doi.org/10.1175/1520-0442(2001)014<1112:GPATFP>2.0.CO;2).
- , and C. Deser, 1999: Diurnal and semidiurnal variations in global surface wind and divergence fields. *J. Geophys. Res.*, **104**, 31 109–31 125, <https://doi.org/10.1029/1999JD900927>.
- , and J. Wang, 1999: Diurnal and semidiurnal tides in global surface pressure fields. *J. Atmos. Sci.*, **56**, 3874–3891, [https://doi.org/10.1175/1520-0469\(1999\)056<3874:DASTIG>2.0.CO;2](https://doi.org/10.1175/1520-0469(1999)056<3874:DASTIG>2.0.CO;2).
- Deser, C., 1994: Daily surface wind variations over the equatorial Pacific Ocean. *J. Geophys. Res.*, **99**, 23 071–23 078, <https://doi.org/10.1029/94JD02155>.
- , and C. A. Smith, 1998: Diurnal and semidiurnal variations of the surface wind field over the tropical Pacific Ocean. *J. Climate*, **11**, 1730–1748, [https://doi.org/10.1175/1520-0442\(1998\)011<1730:DASVOT>2.0.CO;2](https://doi.org/10.1175/1520-0442(1998)011<1730:DASVOT>2.0.CO;2).
- Dipankar, A., S. Webster, X.-Y. Huang, and V. Q. Doan, 2019: Understanding biases in simulating the diurnal cycle of convection over the western coast of Sumatra: Comparison with Pre-YMC observation campaign. *Mon. Wea. Rev.*, **147**, 1615–1631, <https://doi.org/10.1175/MWR-D-18-0432.1>.
- Easterbrook, C. C., 1975: Estimating horizontal wind fields by two-dimensional curve fitting of single Doppler radar measurements. Preprints, *16th Conf. on Radar Meteorology*, Houston, TX, Amer. Meteor. Soc., 214–219.
- Geng, B., and M. Katsumata, 2020: An algorithm for detecting and removing the spurious differential phase observed by C-band polarimetric radar in the rain. *J. Meteor. Soc. Japan*, **98**, 585–613, <https://doi.org/10.2151/jmsj.2020-031>.

- , and —, 2021: Variation of radar-observed precipitation characteristics in relation to the simultaneous passages of a Madden–Julian oscillation event and convectively coupled equatorial waves during the Years of the Maritime Continent pilot study. *Mon. Wea. Rev.*, **149**, 3379–3399, <https://doi.org/10.1175/MWR-D-20-0346.1>.
- , —, and K. Taniguchi, 2020: Modulation of the diurnal cycle of precipitation near the southwestern coast of Sumatra by mixed Rossby-gravity waves. *J. Meteor. Soc. Japan*, **98**, 463–480, <https://doi.org/10.2151/jmsj.2020-026>.
- Gille, S. T., S. G. Llewellyn Smith, and N. M. Statom, 2005: Global observations of the land breeze. *Geophys. Res. Lett.*, **32**, L05605, <https://doi.org/10.1029/2004GL02139>.
- Golub, G. H., and C. F. Van Loan, 1996: *Matrix Computations*. 3rd ed. Johns Hopkins University Press, 694 pp.
- Gutzler, D. S., and L. M. Hartten, 1995: Daily variability of lower tropospheric winds over the tropical western Pacific. *J. Geophys. Res.*, **100**, 22 999–23 008, <https://doi.org/10.1029/95JD01879>.
- Hartten, L. M., and P. A. Datulayta, 2004: Seasonal and interannual variations in the daily cycle of winds over the Galápagos. *J. Climate*, **17**, 4522–4530, <https://doi.org/10.1175/3217.1>.
- Hassim, M. E. E., T. P. Lane, and W. W. Grabowski, 2016: The diurnal cycle of rainfall over New Guinea in convection-permitting WRF simulations. *Atmos. Chem. Phys.*, **16**, 161–175, <https://doi.org/10.5194/acp-16-161-2016>.
- Haurwitz, B., and A. D. Cowley, 1973: The diurnal and semidiurnal barometric oscillations, global distribution and annual variation. *Pure Appl. Geophys.*, **102**, 193–222, <https://doi.org/10.1007/BF00876607>.
- Hersbach, H., and Coauthors, 2020: The ERA5 global reanalysis. *Quart. J. Roy. Meteor. Soc.*, **146**, 1999–2049, <https://doi.org/10.1002/qj.3803>.
- Holton, J. R., 2004: *An Introduction to Dynamic Meteorology*. 4th ed. Academic Press, 529 pp.
- Houze, R. A., Jr., S. G. Geotis, F. D. Marks Jr., and A. K. West, 1981: Winter monsoon convection in the vicinity of north Borneo. Part I: Structure and time variation of the clouds and precipitation. *Mon. Wea. Rev.*, **109**, 1595–1614, [https://doi.org/10.1175/1520-0493\(1981\)109<1595:WMCITV>2.0.CO;2](https://doi.org/10.1175/1520-0493(1981)109<1595:WMCITV>2.0.CO;2).
- Hsu, S.-A., 1970: Coastal air-circulation system: Observations and empirical model. *Mon. Wea. Rev.*, **98**, 487–509, [https://doi.org/10.1175/1520-0493\(1970\)098<0487:CACSOA>2.3.CO;2](https://doi.org/10.1175/1520-0493(1970)098<0487:CACSOA>2.3.CO;2).
- Johnston, B. W., J. D. Marwitz, and R. E. Carbone, 1990: Single Doppler radar analysis of banded precipitation structures. *J. Atmos. Oceanic Technol.*, **7**, 866–875, [https://doi.org/10.1175/1520-0426\(1990\)007<0866:SDRAOB>2.0.CO;2](https://doi.org/10.1175/1520-0426(1990)007<0866:SDRAOB>2.0.CO;2).
- Kilpatrick, T., S.-P. Xie, and T. Nasuno, 2017: Diurnal convection-wind coupling in the Bay of Bengal. *J. Geophys. Res. Atmos.*, **122**, 9705–9720, <https://doi.org/10.1002/2017JD027271>.
- Koch, S. E., and C. O’Handley, 1997: Operational forecasting and detection of mesoscale gravity waves. *Wea. Forecasting*, **12**, 253–281, [https://doi.org/10.1175/1520-0434\(1997\)012<0253:OFADOM>2.0.CO;2](https://doi.org/10.1175/1520-0434(1997)012<0253:OFADOM>2.0.CO;2).
- Koscielny, A. J., R. J. Doviak, and R. Rabin, 1982: Statistical considerations in the estimation of divergence from single-Doppler radar and application to prestorm boundary-layer observations. *J. Appl. Meteor.*, **21**, 197–210, [https://doi.org/10.1175/1520-0450\(1982\)021<0197:SCITEO>2.0.CO;2](https://doi.org/10.1175/1520-0450(1982)021<0197:SCITEO>2.0.CO;2).
- Lane, T. P., and F. Zhang, 2011: Coupling between gravity waves and tropical convection at mesoscales. *J. Atmos. Sci.*, **68**, 2582–2598, <https://doi.org/10.1175/2011JAS3577.1>.
- Lee, J. C. K., A. Dipankar, and X.-Y. Huang, 2021: On the sensitivity of the simulated diurnal cycle of precipitation to 3-hourly radiosonde assimilation: A case study over the western Maritime Continent. *Mon. Wea. Rev.*, **149**, 3449–3468, <https://doi.org/10.1175/MWR-D-20-0423.1>.
- Li, Y., and R. E. Carbone, 2015: Offshore propagation of coastal precipitation. *J. Atmos. Sci.*, **72**, 4553–4568, <https://doi.org/10.1175/JAS-D-15-0104.1>.
- Liang, Z., and D. Wang, 2017: Sea breeze and precipitation over Hainan Island. *Quart. J. Roy. Meteor. Soc.*, **143**, 137–151, <https://doi.org/10.1002/qj.2952>.
- Liu, C., and M. W. Moncrieff, 2004: Effects of convectively generated gravity waves and rotation on the organization of convection. *J. Atmos. Sci.*, **61**, 2218–2227, [https://doi.org/10.1175/1520-0469\(2004\)061<2218:EOCGGW>2.0.CO;2](https://doi.org/10.1175/1520-0469(2004)061<2218:EOCGGW>2.0.CO;2).
- Love, B. S., A. J. Matthews, and G. M. S. Lister, 2011: The diurnal cycle of precipitation over the Maritime Continent in a high-resolution atmospheric model. *Quart. J. Roy. Meteor. Soc.*, **137**, 934–947, <https://doi.org/10.1002/qj.809>.
- Madden, R. A., and P. R. Julian, 1972: Description of global-scale circulation cells in the tropics with a 40–50 day period. *J. Atmos. Sci.*, **29**, 1109–1123, [https://doi.org/10.1175/1520-0469\(1972\)029<1109:DOGSCC>2.0.CO;2](https://doi.org/10.1175/1520-0469(1972)029<1109:DOGSCC>2.0.CO;2).
- Mapes, B. E., T. T. Warner, and M. Xu, 2003: Diurnal patterns of rainfall in northwestern South America. Part III: Diurnal gravity waves and nocturnal convection offshore. *Mon. Wea. Rev.*, **131**, 830–844, [https://doi.org/10.1175/1520-0493\(2003\)131<0830:DPORIN>2.0.CO;2](https://doi.org/10.1175/1520-0493(2003)131<0830:DPORIN>2.0.CO;2).
- Matejka, T., and R. C. Srivastava, 1991: An improved version of the extended velocity–azimuth display analysis of single-Doppler radar data. *J. Atmos. Oceanic Technol.*, **8**, 453–466, [https://doi.org/10.1175/1520-0426\(1991\)008<0453:AIVOTE>2.0.CO;2](https://doi.org/10.1175/1520-0426(1991)008<0453:AIVOTE>2.0.CO;2).
- Minobe, S., J. H. Park, and K. S. Virts, 2020: Diurnal cycles of precipitation and lightning in the tropics observed by TRMM3G68, GSMaP, LIS, and WLLN. *J. Climate*, **33**, 4293–4313, <https://doi.org/10.1175/JCLI-D-19-0389.1>.
- Mori, S., and Coauthors, 2004: Diurnal land–sea rainfall peak migration over Sumatera Island, Indonesian Maritime Continent, observed by TRMM satellite and intensive rawinsonde soundings. *Mon. Wea. Rev.*, **132**, 2021–2039, [https://doi.org/10.1175/1520-0493\(2004\)132<2021:DLRPMO>2.0.CO;2](https://doi.org/10.1175/1520-0493(2004)132<2021:DLRPMO>2.0.CO;2).
- Muñoz, R. C., 2008: Diurnal cycle of surface winds over the subtropical southeast Pacific. *J. Geophys. Res.*, **113**, D13107, <https://doi.org/10.1029/2008JD009957>.
- Ramage, C. S., 1968: Role of a tropical “Maritime Continent” in the atmospheric circulation. *Mon. Wea. Rev.*, **96**, 365–370, [https://doi.org/10.1175/1520-0493\(1968\)096<0365:ROATMC>2.0.CO;2](https://doi.org/10.1175/1520-0493(1968)096<0365:ROATMC>2.0.CO;2).
- Rotunno, R., 1983: On the linear theory of the land and sea breeze. *J. Atmos. Sci.*, **40**, 1999–2009, [https://doi.org/10.1175/1520-0469\(1983\)040<1999:OTLTOT>2.0.CO;2](https://doi.org/10.1175/1520-0469(1983)040<1999:OTLTOT>2.0.CO;2).
- Sakaeda, N., G. Kiladis, and J. Dias, 2020: The diurnal cycle of rainfall and the convectively coupled equatorial waves over the Maritime Continent. *J. Climate*, **33**, 3307–3331, <https://doi.org/10.1175/JCLI-D-19-0043.1>.
- Short, E., C. L. Vincent, and T. P. Lane, 2019: Diurnal cycle of surface winds in the Maritime Continent observed through satellite scatterometry. *Mon. Wea. Rev.*, **147**, 2023–2044, <https://doi.org/10.1175/MWR-D-18-0433.1>.
- Simpson, J. E., 1969: A comparison between laboratory and atmospheric density currents. *Quart. J. Roy. Meteor. Soc.*, **95**, 758–765, <https://doi.org/10.1002/qj.49709540609>.
- Stensrud, D. J., and J. M. Fritsch, 1993: Mesoscale convective systems in weakly forced large-scale environments. Part I: Observations. *Mon. Wea. Rev.*, **121**, 3326–3344, [https://doi.org/10.1175/1520-0493\(1993\)121<3326:MCSIWF>2.0.CO;2](https://doi.org/10.1175/1520-0493(1993)121<3326:MCSIWF>2.0.CO;2).

- Su, T., and G. Zhai, 2017: The role of convectively generated gravity waves on convective initiation: A case study. *Mon. Wea. Rev.*, **145**, 335–359, <https://doi.org/10.1175/MWR-D-16-0196.1>.
- Tan, J., G. J. Huffman, D. T. Bolvin, and E. J. Nelkin, 2019: Diurnal cycle of IMERG V06 precipitation. *Geophys. Res. Lett.*, **46**, 13 584–13 592, <https://doi.org/10.1029/2019GL085395>.
- Tulich, S. N., and B. E. Mapes, 2008: Multiscale convective wave disturbances in the tropics: Insights from a two-dimensional cloud-resolving model. *J. Atmos. Sci.*, **65**, 140–155, <https://doi.org/10.1175/2007JAS2353.1>.
- Uccellini, L. W., and S. E. Koch, 1987: The synoptic setting and possible energy sources for mesoscale wave disturbances. *Mon. Wea. Rev.*, **115**, 721–729, [https://doi.org/10.1175/1520-0493\(1987\)115<0721:TSSAPE>2.0.CO;2](https://doi.org/10.1175/1520-0493(1987)115<0721:TSSAPE>2.0.CO;2).
- Ueyama, R., and C. Deser, 2008: A climatology of diurnal and semidiurnal surface wind variations over the tropical Pacific Ocean based on the Tropical Atmosphere Ocean moored buoy array. *J. Climate*, **21**, 593–607, <https://doi.org/10.1175/JCLI1666.1>.
- Vincent, C. L., and T. P. Lane, 2016: Evolution of the diurnal precipitation cycle with the passage of a Madden–Julian oscillation event through the Maritime Continent. *Mon. Wea. Rev.*, **144**, 1983–2005, <https://doi.org/10.1175/MWR-D-15-0326.1>.
- Waldteufel, P., and H. Corbin, 1979: On the analysis of single-Doppler radar data. *J. Appl. Meteor.*, **18**, 532–542, [https://doi.org/10.1175/1520-0450\(1979\)018<0532:OTAOSD>2.0.CO;2](https://doi.org/10.1175/1520-0450(1979)018<0532:OTAOSD>2.0.CO;2).
- Wang, J.-J., 2004: Evolution and structure of the mesoscale convection and its environment: A case study during the early onset of the Southeast Asian summer monsoon. *Mon. Wea. Rev.*, **132**, 1104–1120, [https://doi.org/10.1175/1520-0493\(2004\)132<1104:EASOTM>2.0.CO;2](https://doi.org/10.1175/1520-0493(2004)132<1104:EASOTM>2.0.CO;2).
- Wei, Y., Z. Pu, and C. Zhang, 2020: Diurnal cycle of precipitation over the Maritime Continent under modulation of MJO: Perspectives from cloud-permitting scale simulations. *J. Geophys. Res. Atmos.*, **125**, e2020JD032529, <https://doi.org/10.1029/2020JD032529>.
- Williams, C. R., and S. K. Avery, 1996: Diurnal winds observed in the tropical troposphere using 50 MHz wind profilers. *J. Geophys. Res.*, **101**, 15 051–15 060, <https://doi.org/10.1029/96JD01013>.
- Wood, R., M. Köhler, R. Bennartz, and C. O'Dell, 2009: The diurnal cycle of surface divergence over the global oceans. *Quart. J. Roy. Meteor. Soc.*, **135**, 1484–1493, <https://doi.org/10.1002/qj.451>.
- Worku, L. Y., A. Mekonnen, and C. J. Schreck III, 2019: Diurnal cycle of rainfall and convection over the Maritime Continent using TRMM and ISCCP. *Int. J. Climatol.*, **39**, 5191–5200, <https://doi.org/10.1002/joc.6121>.
- Wu, P., M. Hara, J.-I. Hamada, M. D. Yamanaka, and F. Kimura, 2009: Why a large amount of rain falls over the sea in the vicinity of western Sumatra Island during nighttime. *J. Appl. Meteor. Climatol.*, **48**, 1345–1361, <https://doi.org/10.1175/2009JAMC2052.1>.
- Yokoi, S., S. Mori, M. Katsumata, B. Geng, K. Yasunaga, F. Syamsudin, Nurhayati, and K. Yoneyama, 2017: Diurnal cycle of precipitation observed in the western coastal area of Sumatra Island: Offshore preconditioning by gravity waves. *Mon. Wea. Rev.*, **145**, 3745–3761, <https://doi.org/10.1175/MWR-D-16-0468.1>.
- Yoneyama, K., and C. Zhang, 2020: Years of the Maritime Continent. *Geophys. Res. Lett.*, **47**, e2020GL087182, <https://doi.org/10.1029/2020GL087182>.